RSC Advances

REVIEW

View Article Online
View Journal | View Issue

Cite this: *RSC Adv.*, 2023, **13**, 17633

Dynamics of reduced graphene oxide: synthesis and structural models

Edwin T. Mombeshora *[a] and Edigar Muchuweni [b]

Technological advancements are leading to an upsurge in demand for functional materials that satisfy several of humankind's needs. In addition to this, the current global drive is to develop materials with high efficacy in intended applications whilst practising green chemistry principles to ensure sustainability. Carbon-based materials, such as reduced graphene oxide (RGO), in particular, can possibly meet this criterion because they can be derived from waste biomass (a renewable material), possibly synthesised at low temperatures without the use of hazardous chemicals, and are biodegradable (owing to their organic nature), among other characteristics. Additionally, RGO as a carbon-based material is gaining momentum in several applications due to its lightweight, nontoxicity, excellent flexibility, tuneable band gap (from reduction), higher electrical conductivity (relative to graphene oxide, GO), low cost (owing to the natural abundance of carbon), and potentially facile and scalable synthesis protocols. Despite these attributes, the possible structures of RGO are still numerous with notable critical variations and the synthesis procedures have been dynamic. Herein, we summarize the highlights from the historical breakthroughs in understanding the structure of RGO (from the perspective of GO) and the recent state-of-the-art synthesis protocols, covering the period from 2020 to 2023. These are key aspects in the realisation of the full potential of RGO materials through the tailoring of physicochemical properties and reproducibility. The reviewed work highlights the merits and prospects of the physicochemical properties of RGO toward achieving sustainable, environmentally friendly, low-cost, and high-performing materials at a large scale for use in functional devices/processes to pave the way for commercialisation. This can drive the sustainability and commercial viability aspects of RGO as a material.

Received 30th March 2023
Accepted 6th June 2023

DOI: 10.1039/d3ra02098c

rsc.li/rsc-advances

[a]*Department of Chemistry and Earth Sciences, University of Zimbabwe, Mount Pleasant, Harare, MP167, Zimbabwe. E-mail: mombeshoraet@gmail.com; emombeshora@science.uz.ac.zw*

[b]*Department of Engineering and Physics, Bindura University of Science Education, Bindura, Zimbabwe*

Edwin T. Mombeshora is a Lecturer in Physical Chemistry in the Department of Chemistry and Earth Sciences, University of Zimbabwe (UZ), Harare, Zimbabwe. He has previously served as an international Technology Transfer Fellow at Swansea University, United Kingdom (2021–2022). He is currently a member of the UZ Quality Assurance Committee, Post-Doctoral Fellow member of the South African Chemical Institute and RSC Affiliate. His research interests include: Materials Chemistry and Nanotechnology. His recent research involvement focuses on the development of carbon-based materials for use as catalysts in biomass-to-platform chemicals conversion, as well as electrodes for solar energy conversion and energy storage.

Edigar Muchuweni is a Senior Lecturer in the Department of Engineering and Physics at Bindura University of Science Education, Bindura, Zimbabwe. He has previously served as Coordinator of the Postgraduate Seminar Series at Botswana International University of Science and Technology (BIUST) (2016–2017). His research interests include: Solar Energy Materials, Nanotechnology and Materials Science. Regarding the latter, his research group works on novel nanomaterials, such as carbon nanotubes, graphene, graphene oxide and reduced graphene oxide, for several applications including energy harvesting, conversion and storage devices.

1 Introduction

Carbon is the basic building block of biomass and is a component of the graphitic framework that constitutes most modern synthetic nanomaterials. With the well-liked potential roles that graphene (an individual sheet of carbon atoms in graphite)[1] can play in the modern world and the associated current industrial scale challenges (that have hindered this progression), it is imperative to shift towards graphene derivatives as alternatives.[2] The importance of graphene in recent materials with high potential in modern applications is highlighted by the fact that graphene is the basic building block of most carbon-based nanomaterials.

1.1 Graphene as the building block

Graphene is a one atom thick 2-D allotrope of carbon comprising of sp^2 hybrids of carbon in a hexagonal morphology.[3–5] Interestingly, graphene was first isolated in 2004 by means of a mechanical "sticky tape" method[3,6] though it has been around for several years as a basic building block of many carbon-based materials.[7] Despite this milestone, processability and industrial scale production of pure graphene in an appreciable exfoliated form is still a challenge as it has been a problem for the longest time, hence, research has shifted to alternatives. The stacking (owing to weak van der Waals forces between sheets), zero band gap and hydrophobic nature of graphene are other essential motivations for seeking alternative materials.[1,8] One closest alternative to graphene is reduced graphene oxide (RGO). Interestingly, RGO is a derivative of graphene and the scalable exfoliation pathway to this material is graphene oxide (GO). The main structural modifications of RGO from pristine graphene are the COOH functionalities that are retained from GO, on the edges, and the topological defects induced by the removal of oxygen moieties upon reduction (Scheme 1).[3,9] Therefore, the current work focused on the review of the synthesis, properties and recent applications of RGO through the possible scalable GO route.

2 Graphene oxide as a pathway to understanding reduced graphene oxide

The pathway to RGO is shown in Scheme 1 and a better understanding of the RGO structure is possible through models proposed for GO. The analogy here is that, since RGO is a form of GO that has some of the oxygen moieties partially removed, the various models that have been put forward to explain GO structure are assumed applicable to RGO. This approach also assumes that there are negligible structural deformations that occurs during reduction.[10]

2.1 Proposed structural models

The structure of GO has been an unresolved phenomenon for a while. Several models have been proposed, however, limitations in explaining certain issues of this family of materials has been realised over time. This is probably because the ultimate composition of RGO is influenced by the starting material, oxidation, and reduction conditions. This work reviews critical examples of key models that have been reported for GO and can be extrapolated to RGO toward future structural solutions. As a start, Matsuo (1994, Fig. 1a)[11] proposed double carbon layers linked to each other by carbon sp^3-bonds that are perpendicular to the carbon network.

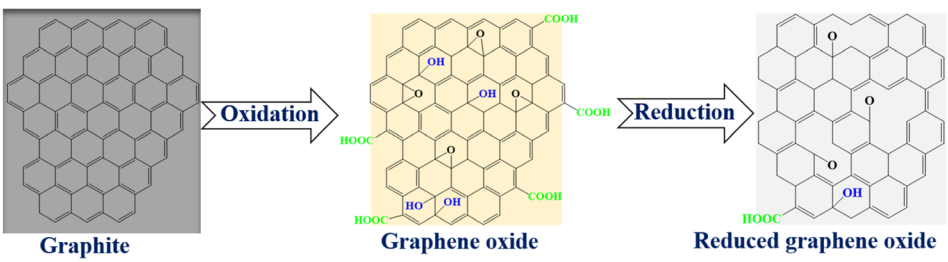

Scheme 1 The illustration of colour changes during exfoliation and reduction to form reduced graphene oxide.

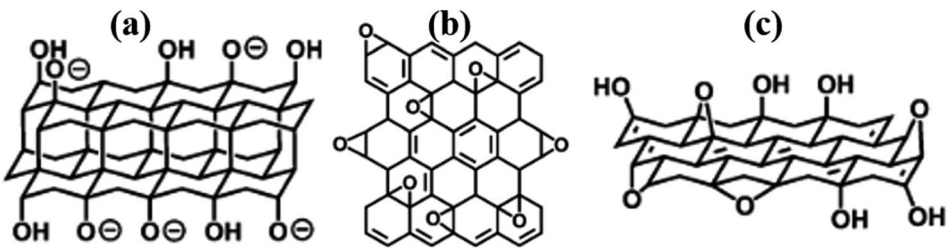

Fig. 1 Some of the early proposed models (a) Nakajima-Matsuo,[11] (b) Hofmann,[12] and (c) Ruess.[13] All reproduced from ref. 14 with permission from the Royal Society of Chemistry, copyright 2014.

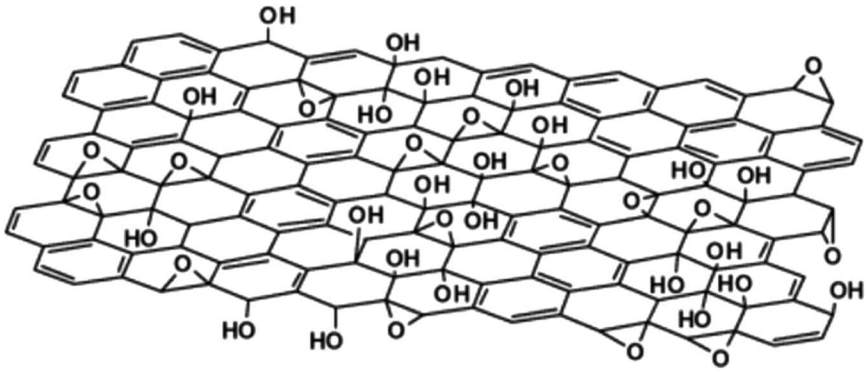

Fig. 2 The proposed Lerf–Klinowski model. Reprinted (adapted) with permission from ref. 15. American Chemical Society, copyright 1998.

The Hofmann (1939) model proposed that GO contained only epoxy groups and that the moieties were distributed throughout the basal plane with a net molecular formula of C_2O (Fig. 1b).[12] The Ruess (1946) model inferred that GO consisted of a basal plane of sp^3-hybridized carbon atoms in a *trans*-linked cyclohexane chair conformation (Fig. 1c).[10,13] The key achievement of this model was the ability to account for H atoms in the GO structure. Despite this key breakthrough, the widely accepted model for GO was reported by Lerf–Klinowski in 1998.[15] This model distinguishes two types of regions in the GO structure, namely, the aromatic region comprising unoxidized benzene rings and the aliphatic region containing six-membered rings with oxygen functionalities (Fig. 2). The model further proposed that the epoxy and hydroxyl groups are located in the basal plane of GO, while the carboxyl, anhydride, lactone, phenol, lactol, and pyrone groups are found in the periphery regions of GO.

Further work in structural modelling saw Szabó *et al.*[16] in 2006 also proposing another model consisting of two regions, namely, translinked cyclohexane chairs and ribbons of flat hexagons made up of C=C bonds and functional moieties, such as 1,3-ether and tertiary hydroxyl groups (Fig. 3). The elucidation of lattice species was a key advancement from the model and provided a further understanding of the GO structure in terms of the observed planar acidity, and corroborated the idea of surface functionalisation during oxidation.

In 2010, Lee *et al.*,[10] proposed a model that was supported by the data from several physicochemical techniques (scanning electron microscopy (SEM), transmission electron microscopy (TEM), X-ray diffraction spectroscopy (XRD), Fourier transform-infra red spectroscopy (FT-IR), X-ray photoelectron spectroscopy (XPS), Carbon-13 (^{13}C) solid-state nuclear magnetic resonance (NMR) and X-ray absorption near edge structure (XANES)) in that GO consists of amorphous carbons (sp^3-hybridised carbons) and crystalline carbons (sp^2-hybridised) (Fig. 4). The strength of the model was in accounting for stability in GO by

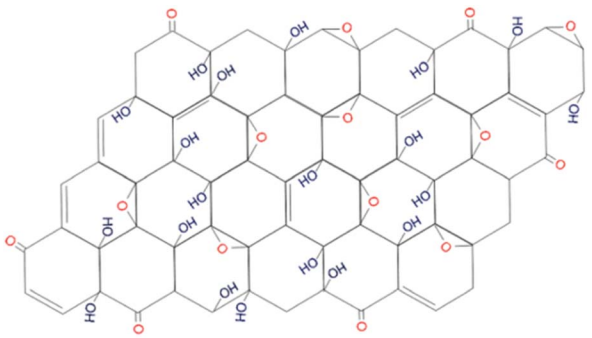

Fig. 4 The model proposed by Lee *et al.*, in 2010. Reprinted (adapted) with permission from ref. 10 American Chemical Society, copyright 2010.

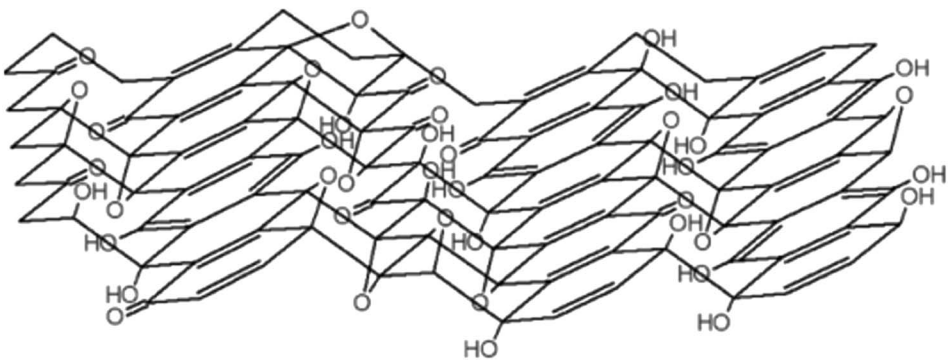

Fig. 3 The model proposed by Szabó *et al.*, Reprinted (adapted) with permission from ref. 16. American Chemical Society, copyright 2006.

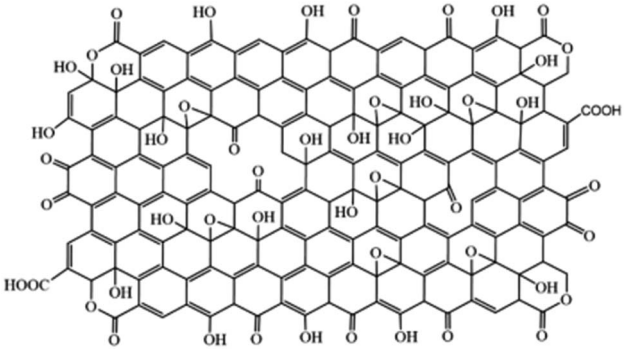

Fig. 5 The model proposed by Aliyev *et al.*,[17] in 2019. Reprinted (adapted) with permission from Nanomaterials, copyright 2019.

suggesting the location of hydroxyl groups in opposite sites and far from epoxy moieties.[10]

Again, in 2019 Aliyev *et al.*,[17] proposed a model that uniquely suggested replacing C with O in GO (Fig. 5). This model supports most of the reported structures of GO.

Brisebois and Siaj[18] proposed a model that accounted for carbon vacancies, carbon radicals, C/O ratio of ~2, carbon

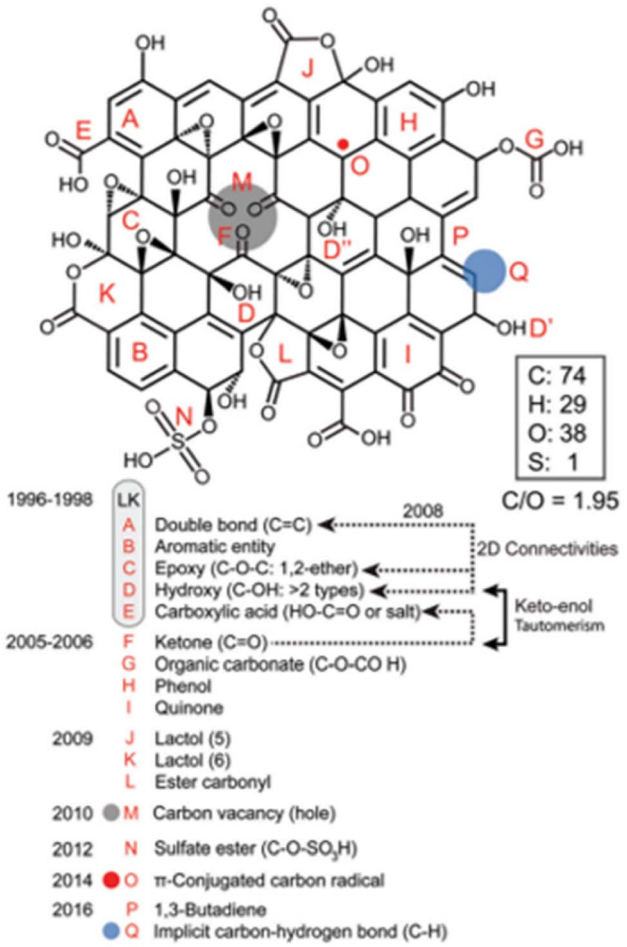

Fig. 6 The model proposed by Brisebois and Siaj. Reproduced from ref. 18 with permission from the Royal Society of Chemistry, copyright 2020.

esters and allylic alcohols (Fig. 6). This model would be more applicable to RGO as well.

2.2 Concerns from the existing structural models

The consensus amongst the various models and experimental data is that the GO-based structures consists of amorphous and crystalline phases. Characterization techniques have also displayed critical common inferences. For instance, GO spectra from the ^{13}C solid-state (NMR) infer the existence of –OH and –O– moieties at 60 and 70 ppm, respectively, while the FT-IR data tend to support this deduction.[10,19] The FT-IR also implies the existence of ketone functionalities which corroborate with XPS, ^{13}C solid-state NMR and O K-edge XANES.[10,20] However, there are several issues associated with each proposed model. From the early models, the Hofmann model does not support existence of other moieties since the model proposed epoxy groups only that were distributed across the basal plane with a net molecular formula of C_2O with no account for H atoms. Additionally, the structure proposed in the Ruess model is not supported by characterization techniques. This is because the model suggested an sp^3-hybridized basal plane structure but several techniques, such as XPS, supports the existence of an sp^2-hybridized system and presence of C=O which are unaccounted for in this model. On the other hand, later models also have shortfalls. For instance, the Nakajima-Matsuo model relied on the assumption of a lattice backbone similar to poly(dicarbonmonofluoride)$(C_2F)_n$ but this hypothesis is yet to be proven and is most probably unstable since carbonyl functionalities with partial negative charges are feasibly stable when coordinated to three other carbon atoms.[16]

The latest models in an attempt to address gaps from earlier models have brought other drawbacks with them. To start with, the Lerf–Klinowski model suggests that carboxyl groups are located at the edges, however, this contradicts the NMR data which do not provide evidence that supports the existence of the moiety (absence of peak near 175 ppm).[10] The Lerf–Klinowski model also lacks an account of the dependence of GO on the starting material, oxidant and oxidation conditions.[21] Despite the provision of a possible explanation to the obtained ^{13}C spectrum by Lee *et al.*,[10] *i.e.*, the fact that the NMR data is misleading due to cross-polarization induced by the fact that carboxyl moieties contains hydrogen, issues in their proposed model are the hydroxyl groups are located too close to each other, hence, infers a possibility of unfavourable electrical instability in the structure. The problems associated with the proposals by Szabó *et al.*,[16] are linked to the existence of cyclohexane chair conformations which still lacks satisfactory experimental evidence and the model does not account for the existence of other moieties. Furthermore, the shortfall of the model proposed by Lee[10] is the exclusion of carboxyl and lactone groups in the structure, since the solid-state ^{13}C NMR data show the existence of both functionalities. Brisebois and Siaj[18] ignored the convention that in line diagrams, carbon and hydrogen atoms may not necessarily be drawn in estimating and deducing the shortfalls of earlier models before presenting their proposed structure. To sum up, the modelling for RGO

structure still needs more insights. The variations causing most shortfalls have a foundation in precursor materials, *i.e.*, GO materials synthesised by several methods.

2.3 Summarised synthesis methods

Readers are referred to detailed reviews by Ikram *et al.*,[22] Brisebois and Siaj.[18] and Dong *et al.*[23] on GO synthesis. In brief, synthesis methods can be classified in two broad classes. The first category can be referred to as chlorate methods and examples of this class include the Hofmann and Staudenmaier methods (additionally involving the use of HNO_3),[24,25] and the Brodie (based on additional use of HNO_3 and H_2SO_4). The second class is the most popular and can be referred to as permanganate methods. This class is associated with higher levels of oxidation. The most common examples are Hummers (and several modified Hummers methods)[26] and Offeman methods, which are based on H_2SO_4 and $NaNO_3$ additives. Another recent example is known as the Tour method (and derivatives) and these methods involve a combination of H_2SO_4 and H_3PO_4 acids as additives. The tailoring of physicochemical properties of GO is mostly through varying the synthesis method and several critical parameters summarised in Table 1. For instance, zeta potential of GO was tuned to approximately −50, −49, −48, −43 and −33 mV (with corresponding C/O ratio of 1.47, 1.59, 1.62, 1.64 and 1.69, respectively) by adding 0, 10, 20, 30, 40 cm^3 of H_2O_2, respectively.[27] Despite the terminating role through elimination of residual MnO_4^{2-} and MnO_2 (conversion to $MnSO_4$), excessive H_2O_2 may cause structural transformations due to creation of substantial π-conjugated carbon radicals in GO (due to reaction of $^{\bullet}OH^-$, from the H_2O_2, with the C=C in the disrupted π-conjugated plane of GO).[27] This suggests that future modified synthesis protocols must either use small quantities or avoid adding large arbitrary volumes of H_2O_2 that are not systematically determined. Also, the surface area of GO was tuned from 2 to 8 and 185 $m^2\ g^{-1}$ (with corresponding C/O ratios of 0, 1.67 and 1.48, respectively) by varying graphite (starting material): Na_2NO_3 ratios in the 1 : 0, 2 : 1 and 1 : 1 fashion, respectively.[28] In a similar study involving carbon nanoplates, lattice sizes of 8.72, 7.38 and 4.84 nm (with corresponding C/O ratios of 0.87, 0.95 and 0.86, respectively) were obtained by changing carbon nanoplatelets (CNP, starting material): Na_2NO_3 ratio of 1 : 0, 2 : 1 and 1 : 1, respectively.[20] In the same study, CNP : $KMnO_4$ ratios (1 : 0, 1 : 3, 1 : 6, 1 : 9, 1 : 12) were used to tailor the ratios (4.08, 1.48, 1.16, 0.87 and 0.78, respectively). One of the common critical weaknesses of oxidation protocols is the associated aggressiveness, which may introduce unrequired chemical functionalities and contamination from residual reagents.

Graphite oxidation involves an initial defect generation followed by oxidation at defect sites. The theory has predicted that the main oxygen moieties found at these defect sites are ketones and quinones.[17] However, depending on the size of the defects created during oxidation and impurities introduced into the carbon framework, other chemical moieties can also be formed. For instance, sulfur impurity from the permanganate method can be chemically linked to the carbon backbone.[17] These are aspects that need to be considered critically in further shaping of current models of RGO. There seems to be a consensus, based on the widely accepted model,[15] on the locations of the phenolic (–OH) and epoxy (C–O–C), and acidic groups (–COOH) in the basal plane and edges, respectively.[8] Hence, the basal planes of RGO sheets are assumed to be basic, whilst their edges are acidic, suggesting an amphoteric characteristic.

Possible mechanism behind popular permanganate methods:[12,34]

$$KMnO_4 + 3H_2SO_4 \rightarrow K^+ + MnO_3^+ + H_3O^+ + 3HSO_4^- \quad (1)$$

$$MnO_3^+ + MnO_4^- \rightarrow Mn_2O_7 \quad (2)$$

$$Mn_2O_7 + C_{(graphite)} + H_2SO_4 \rightarrow C\text{-}Oxy + MnO_5 + H_2O + SO_4^{2-} \quad (3)$$

The intentional introduction of oxygen-containing moieties on the surfaces of graphite often culminate in the increment of distance between layers from the usual 0.34 nm due to exfoliation initiated by repulsions between functionalised sheets (oxygen has an electronegativity of 3.44 greater than 2.55 of carbon).[10,35] The Na^+, from the added $NaNO_3$ in most versions of the Hummers' method, has been reported to also have an intercalation effect during oxidation (through the mechanism in eqn (4)–(6)), thus, further increase the *d*-spacing by disrupting π–π interactions.[17,28]

$$C_{(graphite)} + NaNO_3 \rightarrow CNaNO_3 \quad (4)$$

$$4KMnO_4 + 2H_2O \rightarrow 4KOH + 4MnO_2 + 3O_2 \quad (5)$$

$$CNaNO_3 + nO_2 \rightarrow GO \quad (6)$$

3 Reduced graphene oxide

RGO can be considered an intermediate material with few oxygen-containing moieties than the parent GO and is obtained during reduction towards restoration of the original conjugated system of graphene (Scheme 1).[4,36] RGO has captured interest of several researchers in wide-ranging fields due to its cost-

Table 1 Critical key reaction parameters in GO synthesis towards tailoring properties of RGO

Reactions conditions[21,29]	Starting material[12,30]	Other reagents added
Time[10]	Size[31,32]	Oxidant strength[17,21]
Temperature[33]	Shape[31]	Acid concentration[17]
Mixing rate and mode	Surface area[21]	Mixing ratio[20,28]
		Terminating reagent[27]

effectiveness, large-scale production, and relatively ease of synthesis, and several other attributes discussed in the following sections.

3.1 Properties

Future applications can be driven by the currently established physicochemical properties that are, in turn, influenced by defects and holes induced by missing carbon atoms, type, and distribution of residual oxygen functionalities per RGO lattice.

3.1.1 Chemical structure. The sp^2-hybridized C–C σ-bond in RGO framework has a bond length of ∼0.142 nm.[7,37] The removal of oxygen moieties cause structural variations in the form of lattice deformations from introduced dopants or created vacancies, and this in turn induces chemical modifications.[38] Since the most common oxygen-containing moieties on the surface of GO are OH, C–O–C, –COOH and C=O, reduction minimises their content but retains surface polarity and exfoliation in aqueous-media.[3,39] The residual oxygen-containing functionalities on the sheets of RGO allow interaction with metal ligands, and thus allow chemical linkage of metal oxides in most composites.[40] The chemical composition of RGO is controlled by precise synthesis protocols and the C/O ratio in most reports is ∼12.[17] The combination of polarised RGO surfaces and hydrophobic sp^2 hybridized graphitic basal planes brings amphiphilic traits to the material.[41] Hence, both covalent (through oxygen moieties) and noncovalent interactions (*via* electrostatic and π–π interactions with cations and other conjugated backbones, respectively) are possible routes to further modify RGO.

3.1.2 Morphology and mechanical properties. The layered structure (with intrinsic wrinkles) and mechanical stability (Young modulus: ∼1 TPa and tensile strength: ∼130 GPa) are some of the key motivations behind the current attention on RGO materials.[42–45] The RGO by chemical means has outstanding stress transfer capabilities.[46] The zigzag morphology on RGO edges renders the material with weak ferromagnetic properties.[47] In addition, the mechanical strength of RGO can be rationalised by the strong C–C σ-bonds.[3,9] Furthermore, residual oxygen-containing groups make RGO more compatible with other organic materials in composites than graphene through a considerable transformation from van der Waals to chemical interactions.[48–51] This ultimately enhances mechanical properties. For instance, Monteserín *et al.*[48] reported an improved glass transition temperature and storage modulus of epoxy using RGO additives *via* possible covalent linkages that enhanced crosslinking density and rigidity. Another possibility from this report could be that oxygen groups also facilitate high mechanical strength by aiding dispersibility. Similarly, Yan *et al.*[50] reported an ∼62% increase in fracture toughness of a geopolymer upon the addition of 5 wt% of RGO. In another study, Kiamahalleh *et al.*[52] reported RGO sheet sizes of 170 nm that showed better tensile and compressive strengths in cement composites than when RGO sheets with sizes of 245 nm were used. This means that RGO traits have progressed to tune mechanical properties of other materials through compositing and this was approached not only on the basis of high aspect ratios, but also on the considerations of sheet sizes and composition of oxygen functionalities. A reported density functional theory simulation concluded that hydroxyl and epoxy moieties of RGO induce brittle and ductile characteristics, respectively.[53] Practical studies on the effect of reductants on specific oxygen species and content, and in turn the application of reduction protocols in tuning mechanical properties are still lacking in the current literature, and a focus in this direction has the potential to enable further developments of RGO-based materials.

On the other hand, other studies have pointed out the decrease in mechanical properties owing to oxygen moieties.[53] For example, oxygen functionalities were reported to have lower mechanical attributes in cementitious composites when compared to graphene.[49] Additionally, a study through molecular dynamic simulations on the impact of wt% of oxygen groups on the mechanical properties of RGO revealed that an increase from 10 to 50% triggered severe deterioration of stress (from 110 to 55 GPa) and elastic modulus (from 0.5 to 0.3 TPa).[54] The same work concluded that hydroxyl and epoxides induce easy fracturing effects on sheets due to weakened C–C σ-bonds in the diamond-like structures of RGO (relative to the C=C honeycomb structure in pristine graphene).[54] In a similar study, molecular dynamic simulations showed that high coverage of sheet surfaces with epoxides was associated with high ripple density and longer bond lengths that were in turn detrimental to mechanical strength.[55] This common contradiction most likely suggests that RGO composition improves mechanical properties up to an optimum value and thereafter causes a deteriorating effect. Another feasible rationale for the inconsistencies is the widespread characteristics emanating from a wide range of synthesis methodologies and precursor materials. Therefore, as a future research direction, more focus on practical studies can probably clarify these differences. RGO is usually restacked and more agglomerated than GO (as often depicted by microscopy techniques (darker micrographs) and XRD).[56,57] Additionally, recent studies have deduced high surface areas as one of the key features that affect mechanical properties through high dispersibility of other composites components,[49,50] hence, this deduction suggests that GO is better than RGO as a mechanical reinforcement agent.

3.1.3 Electrical and thermal conductivity. The utilisation of RGO instead of GO (bandgap ∼2.2 eV)[58] in electronic applications is mostly driven by the approximate four-fold enhancement of conductivity (as high as 57 300 S m^{-1})[8] in the reduced form. The partially restored π-system in RGO lowers the band gap.[12,59] For example, Olumurewa *et al.*[60] lowered the band gap from 2.4 to 1.5 eV by reducing GO with $NaBH_4$. Although residual oxygen moieties, structural defects and vacancies that are generated during reduction of GO lessen conductivity of ultimate RGO relative to graphene (84 500 S cm^{-1}), the bulk conductivities of some RGO falls within the useful ranges.[12,44,61] On the other hand, defects and grain boundaries in RGO raise phonon scattering and in turn lower thermal conductivity to ∼2.96 W m^{-1} K^{-1} relative to that of graphene (∼5000 W m^{-1} K^{-1}), consequently, RGO performs better than graphene in thermoelectric generators.[7,44,61] Also, higher electron mobility in

RGO than in GO[62] minimises chances of recombination of photoinduced electron–hole pairs.[59,63] Additionally, RGO has an inherited high electron mobility than spherical nanomaterials by virtue of a 2-D morphology that is attributed to condensed junctions and grain boundaries.[64,65] Excessive defect intensity may disrupt functionality in some applications, such as piezoelectric applications, as it interferes with electron transport. Nitrogen doping into the carbon framework of RGO has been reported to improve interfacial electron transfer in RGO, and therefore the conductivity increases as nitrogen atoms contribute to the additional electron.[66,67]

3.1.4 Thermal properties. Upon exposure to heat and air, the COO^- in COOH groups on the surfaces of RGO sheets is easily transformed to CO and CO_2.[10,12,15,20] Some authors have proposed that typical graphene derivatives start decomposing slowly above 60–80 °C[16] and this is probably due to the highly disordered mixture of residual oxygen moieties.[12] On the one hand, the weight loss due to thermal decomposition in the air within the range of 125–300 °C is attributed to pyrolysis of oxygen-containing moieties, while that in the range of 300–700 °C is ascribed to the sp^2-hybridised carbon backbone.[33,62,68,69] On the other hand, the weight losses below 100 °C and within the 150–400 °C, 400–500 °C, 650–700 °C and 100–900 °C ranges during pyrolysis under inert conditions have been attributed to trapped water, COOH moieties, lactones, phenols and total oxygen-containing groups on the sheet surfaces, respectively.[19,20,69] The total amount of oxygen functionalities often decreases with increase in pyrolysis temperature in an inert environment,[70] hence, pyrolysis temperature can suitably be manipulated to tune composition in terms of oxygen moieties. In addition, the ultimate surface area and porosity traits of RGO were reported to increase with a rise in pyrolysis temperature, under inert atmospheric conditions, owing to generated oxygen vacancies that are available for nitrogen sorption.[19] The work by Bargaoui *et al.*[39] has shown that OH moieties in H-bonds are preferentially pyrolyzed in hydrazine better than the C–O functionalities in epoxides. The same study has also hinted that the decline in OH groups after pyrolysis is a common oversight in most reports due to water contamination (intercalated water) owing to the hygroscopic nature of RGO. The actual OH functionalities attached to the RGO sheet surface must be carefully distinguished from the non-bonded intercalated water by careful drying before relevant analysis. Doping and surface functionalisation of the carbon framework during pyrolysis in reducing solutions under inert conditions, particularly in hydrazine and urea,[71,72] are unavoidable along with the reduction process.

Due to lower oxygen content and often improved crystallinity (restoration of conjugated system), RGO is generally expected to have a higher thermal stability than GO but lower than that of graphene. However, this trend is dynamic since the thermal stability of RGO-based materials depends on combination of factors such as, number of graphitic sheets, size, residual oxygen functionalities and associated defects.[73] For example, on the one hand, thermal stability would be expected to decrease as the lattice domain sizes of RGO declines due to the induced tearing effect during oxygen removal and on the other hand, the low oxygen content of RGO would be anticipated to induce higher thermal stabilities.[62,68,71,73] Hence, thermal analysis through thermogravimetric analysis is a potential industrial-scale technique for establishing RGO quality in future developments.[73]

3.1.5 Optical and textural properties. Reduction of GO culminates in the red-shifting of the $\pi \rightarrow \pi^*$ peak at ~230 nm (Tables 3–5) ascribed to the C=C bond.[74] Hence, UV-vis spectrophotometry is a suitable technique to determine effective reduction. Also, RGO is attractive due to its strong NIR absorption[75,76] and optical attributes (excellent optical transparency of ~98%)[7,37] that enable use in optics,[77–79] electronics,[80] photovoltaics[81] and photocatalytic reactions[59] (Table 2). The transmittance of RGO decreases with an increase in number of layers,[7,81] hence, reduction optimisation must be pursued as a future research direction for optical needs since reduction may induce agglomeration of layers and different structural parameters. This is imperative because ultimate structural characteristics and film thickness of RGO influence optical band gap values.[39] In addition, the rich oxygen located on surfaces and edges (hydroxyl, carboxyl and epoxy), delocalized π–π electrons (due to restored aromaticity) and large surface of RGO enhance intercalation/adsorption of aromatic organic pollutants that can be photocatalytically degraded, particularly in composites with semiconductors.[10,82–85] Since oxidation is known to enhance the optical band gap energy (in GO relative to graphene), reduction towards a more graphene-like material (in RGO) infers a lower optical band gap energy. This may be rationalised to mean that RGO would be more appropriate for photocatalysis than GO despite a lower content of oxygen functionalities. However, RGO may not reach its maximum adsorption capacity due to possible shrinkage of surface area induced by aggregation from the closer interplanar interaction of graphene sheets after reduction.[86] Also, carbon vacancies generated during reduction of GO form carbon nanoclusters that transform the material towards semiconducting and luminescence (*via* promotion of percolation pathways among clusters) traits that are inclined to chain/cluster sizes/fractions.[64] In this regard, the tuneable textural characteristics and large surface areas offered by RGO are critical in photodegradation, since organic pollutants principally degrade on semiconductor surfaces.[64,87] RGO can be applied as catalyst supports and the 2-D π–π system on its surface facilitates activity of anchored nanoparticles by serving as electron acceptors.[5] Quantum dot form of RGO (RGO-quantum dots) are 0-D materials that display unique characteristics, which emanate from the quantum confinement effect and pronounced edge effects that are inclusive of tuneable band gaps and photoluminescence (PL) with size variations.[88,89]

3.2 Recent applications

RGO as a material has wide-ranging applications[9] and Table 2 highlights some interesting but yet to achieve commercial value. The purpose of the reviewed works in this section is to point out potential areas toward which the material can be fostered. Interestingly, 'certain defects' from the reduction

Table 2 Potential RGO application examples (2020 to 2023)

Application	Example	Ref.
Smart containers	Polymer–RGO composites were used to build smart containers that controlled the desorption of inhibitors and acted as dual passive and active anticorrosive agents	90
Nanofluids	The Al_2O_3–RGO composite achieved a thermal conductivity of 2.076 W m K^{-1} at 45 °C and a heat transfer coefficient of 5462 W m^{-2} $°C^{-1}$ at the exit of the test section that used 0.05 vol% of nanofluid at Reynolds number of 7510	98
Anticorrosive coatings	The polydopamine nanoparticles–RGO composite improved the anticorrosion performance of a waterborne epoxy coating by triggering pH-sensitive activities upon acidic exposure. The composite also displayed self-repairing traits that improved corrosion resistance during long-term exposure by producing an impermeable barrier that delay the electrolyte penetration	99
Electrochemical capacitor electrodes	Polyaniline–N-RGO composite improved specific capacitance by 14 032% (at 50 mV s^{-1}) and 4749% (at 5 mV s^{-1}) compared to performance of pristine N-RGO and PANI in K_2SO_4, respectively	62
Sodium ion battery electrodes	The Ni_3S_2–N-RGO composite showed stable reversible capacity (299.2 mA h g^{-1} for up to 100 cycles at 0.1 A g^{-1}) and coulombic efficiency of ~77%	100
Thermoelectric materials	WO_3–RGO nanocomposite attained ~9-, 14- and 2-fold improvement in figure of merit at 313 K, electrical conductivity and lowering of thermal conductivity relative to pristine WO_3	80
Piezoelectric energy harvesting	A 2% wt% RGO in a room temperature vulcanised silicone rubber–RGO composite lowers the tensile strength to 0.1 MP and increases the fracture strain by 100 times and electrical conductivity	46
Sensors	Polypyrrole–RGO materials were able to quickly and selectively sense NH_3 linearly at room temperature	101
Nano-carrier for cancer treatments	The chitosan-Fe_3O_4–RGO nanocomposite was applied in the targeted delivery of anticancer drug (curcumin) for the suppression of MCF-7 breast cancer cells using the facile water-in-oil emulsification protocol	102
Antibacterial agents	The covalently conjugated peptide–RGO composite displayed improved antibacterial activity against *E. coli* and also achieved a decreased in hemolysis	103
Nanofiltration membranes	The RGO-based membranes achieved a water permeability of 225 L m^{-2} h^{-1} bar^{-1} and a selectivity of 98% in size-exclusion during separation of methyl blue separation. Size and charge are central to this technique	104
Fuel cells	MoS_2–Ni_3S_2–RGO displayed catalytic efficiency and stability of 106 and 104% after 200 uninterrupted cyclic voltammetry cycles for CH_3OH/CH_3CH_2OH electro-oxidation, respectively. The RGO enhanced the specific surface area and electrical conductivity of the electrocatalyst	105
Lithium-ion batteries	Ni-α-MnO_2–RGO anode achieved excellent rate capability (from 0.2 to 10 C), a coulombic efficiency of ~99% and capacity retention of 615 mA h g^{-1} at 830 mA g^{-1} after 200 cycles. The small sizes of α-MnO_2 improved dispersion in the RGO matrix and consequently improved electrical-ionic conductivity, low charge transfer resistance and alleviates volume expansion	106
Lithium–sulfur batteries	Sulfur–RGO cathode attained a specific capacity of 1265 and 903 mA h g^{-1} after the first and hundredth cycles at 0.2 A g^{-1}, respectively owing to improved electronic conductivity from ~10^{-6} to ~0.039 S cm^{-1}	107

effect and doping, as well as composites tune the material for certain applications that could not have been possible with GO and graphene. For instance, the induced hydrophobic nature is advantageous when used as an anti-corrosion material.[90] Also, raised conductivity and N-doping in RGO enhances the applicability in electrochemical capacitors.[71] Additionally, the restored π–π restacking structure in RGO aids high loading of hydrophobic drugs in drug carrier applications (Table 2).[91] In addition to the induced properties of RGO through derivatisation,[92] inherited attributes are also motivations of the recent usage of RGO. To illustrate this point, the nontoxicity and biocompatibility attributes, emanating from the main elemental component, carbon, allow the application of RGO in brain tumour treatments.[93] Also, the semiconducting nature has given RGO promising prospects in sensors.[94] In addition, the conductive nature of RGO and related surface roughness hinder bacterial growth, hence, can be applied for antibacterial activities.[95]

Most of the recent applications reported with potential to achieve commercial value involve the use of RGO in composites

Table 3 Chemical synthesis methods for RGO

	Reduction conditions						
Reductant	GO : H_2O ratio	GO : reductant ratio	Mixing time (h)	Temp (°C)	Reaction time (h)	Comment	Ref.
Aatriplex halimus leaves extract	1 : 5	1 : 2	0.5	80	8	Reduction introduced wrinkles and XRD broad peak at ~22°	117
Azadirachta indica leaf extract	—	2 : 1	1.33	90	2	NaOH adjusted pH to 10 and has reducing effects. Colour change from dark brown to dark black, raised C/O ratio from 2.2 to 5.9, the (002) plane peak at $2\theta \sim 24°$ with corresponding *d*-spacing of ~0.37 nm (decline from ~0.77 nm)	116
Clinacanthus nutans leaf extract	1 : 1	1 : 1	1	100	—	Heating in an oil bath and also at 60 and 80 °C. The OH^- removal and XRD peak $2\theta \sim 22°$ with a *d*-spacing of 0.40 nm were the signatures	118
Eclipta prostrata	1 4	5 : 2	2	Room	—	Surface roughness was an indicator of reduction, GO (14.29 nm) > RGO (2.051 nm) > graphite (1.784 nm)	56
Green tea extract	—	2 : 1	0.75	60	6	The UV-vis peak shifted from 240 nm to ~270 nm. Phytomolecules in green tea extract also functionalised the RGO surface	125
Green tea extract	12 : 5	6 : 5	2	95	24	Reflux with extract at 95 °C for 24 h produced RGO with a high surface area of 973 $m^2\ g^{-1}$	114
Green tea extract	1 : 2	1 : 100	—	80	8	Reduction was done at a lower temperature and in a conical flask different from the sealed autoclave in most reports	124
Chenopodium album	1 : 1	1 : 10	—	100	12	Reductant also acts as a stabilising agent. Reflux for 12 h at 100 °C was facile and cost-effective	120
A. Cruentus extract	—	10 : 1	—	80	0.75	The freshly prepared aqueous extract was mixed by stirring at 300 rpm. The XRD peak at $2\theta \sim 24°$ was ascribed to the plane (002) of the RGO in the composite	132
H_2CO_3 (from the coca-cola classic drink)	—	4 : 25	—	90	2	Red-shifting of UV-vis peak for π–π* electron transition indicates restoration π-system when the soft drink was added	133
Terpenoids and polyphenols	—	10 : 1	—	70	1	After evaporation of the solvent, the product was separated from the reductant by adding H_2O_2. Reducing and capping agents extracted from *Vernonia amygdalina*, hence, "greener" and sustainable	35
Tecoma stans	1 : 1	1 : 1	1	70	12	The C/O ratio decreased with increase in extract concentration	134
Olea europaea (olive extract)		2 : 1	0.17	—	2	After refluxing for 2 h, UV-vis absorption peak shift from 235 to 276 nm signalling restoration of conjugation upon reduction	121
$Na_2O_4S_2$	—	—	—	90	1.5	The sheet *d*-spacing was 0.38 and 0.36 nm after treatment with $Na_2O_4S_2$ and further with H_2SO_4, respectively	76
$NaBH_4$	2 : 1	—	1	100	1	The lower FTIR peak intensities resulting from oxygen groups were used to confirm their removal	38
$NaBH_4$, CH_3CH_2OH, NH_3	10 : 1	50 : 3	1.5	150	18	NH_3 (25%) slowly added for pH adjustment to ~10. Red-shifting of UV-vis peak from 300 to 260 nm indicated electronic conjugation recovery	135
$NaBH_4$, NaOH	2 : 1	—	7	30	0.67	Reaction was kept at 50 °C till $NaBH_4$ step and under a N_2 atmosphere up to NaOH addition followed by the addition of H_2O_2. Long method, involving a mild heating	96
$NaBH_4$	1 : 1	1 : 1	1.5	Room	—	UV-vis absorption maxima at 303 nm were ascribed to π–π* transitions due to restoration and redecorating of the aromaticity after reduction	136

Table 3 (*Contd.*)

	Reduction conditions						
Reductant	GO : H_2O ratio	GO : reductant ratio	Mixing time (h)	Temp (°C)	Reaction time (h)	Comment	Ref.
$NaBH_4$	—	—	—	—	—	Reduction induced in a controlled N_2 atmosphere at 20 Pa. The chamber was vacuumed to ~10–2 Pa before filling with N_2	137
$C_8H_{11}NO_2 \cdot HCl$	—	1 : 2	—	Room	24	Vigorous stirring at room temperature for 24 h induced reduction without heating, hence an energy-saving approach	138
$C_6H_8O_6$	—	—	—	95	—	Ascorbic was added dropwise under magnetic stirring and reaction time not specified	25
$C_6H_8O_6$	—	1 : 4	—	95	3.5	The assumption of the C_2O as the chemical formula used to deduce the molar mass of GO as 40 g mol^{-1} in this report may not be true according to the proposed models. The XPS C/O ratio increased from 1.98 to 4.47 upon reduction	139
$C_6H_8O_6$	1 : 1	3 : 10	—	80	1	The broad peak at $2\theta \sim 22°$ was attributed to the diffraction peak of RGO	69
$C_6H_8O_6$	~5 : 1	~1 : 1		95	1	The broadened XRD peak at $2\theta = 24°$ and *d*-spacing of ~0.37 nm (greater than 0.34 nm of graphite) indicated RGO. Water contact angle of 44° (<90°) for the RGO inferred hydrophilicity	103
$C_6H_8O_6$	—	—	—	50	12	Reductant amount nor provided and reduction was verified optically with a dark brown/light yellow to black colour change	140
$C_6H_8O_6$	5 : 1	1 : 5	0.17	90	2.5	Sonication was at 600 W for 0.17 h. XRD broad peak at $2\theta \sim 25°$ and C/O ratio of 2.22 (increase from 1.34) signalled RGO formation with a surface area of 176 m^2 g^{-1}	5
$C_6H_8O_6$	5 : 1	1 : 8	1.67	80	24	Chemical and reflux treatments led to disappearance of the XRD signature peak for GO at 2θ ~12° and decline of *d*-spacing to 0.35 nm (from 0.73 nm)	141
$C_6H_8O_6$, NH_3	2 : 3	1 : 10	1.17	85	1.5	NH_3 (25%) was added dropwise to adjust pH to 12. Ascorbic acid is a green reductant and, the disappearance of IR peaks due to oxygen-containing moieties occurred after reduction	44
$C_6H_8O_6$	15 : 4	1 : 67	—	—	48	Irradiation done after adding reductant at 405 nm. Radiation time effect was studied, increase in time led to increased elimination of OH^- (48 h raised C/O ratio from 3.44 to 4.35)	112
$NH_{3(aq)}$, NH_2NH_2	1 : 9	—	0.5	90	—	$NH_{3(aq)}$ was added as an exfoliating agent though it also has reducing effect. The NH_2NH_2 amount was not given	142
$NH_{3(aq)}$, NH_2NH_2	1 : 15	50 : 1	2	90	—	Broad (002) plane at $2\theta = 24°$ and *d*-spacing of 0.44 nm were indicators of reduction	74
NH_2NH_2, KOH	—	—	2	100	24	Chemical and reflux reduction signalled by the $\pi \rightarrow \pi^*$ UV-vis peak shift from 230 to the 260 nm due to reduction and restoration of the conjugated structure (increased π-electron concentration)	43
$NH_2NH_2 \cdot H_2O$, NaOH	10 : 1	200 : 1	0.5	60	4	pH adjustment to 10 by adding either HCl (0.1 N) or NaOH (0.1 M). Highly wrinkled and irregular structured sheets with corrugated surfaces was ascribed to reduction	83
$NH_2NH_2 \cdot H_2O$, $Al(OH)_3$	10 : 1	500 : 1	1.15	90	0.75	Heating was by means of a water bath. Darkened dispersions with a strong-sharp UV-vis peak at ~258 nm signalled completion of reduction and restoration of the conjugated structure of C=C	143

Table 3 (*Contd.*)

Reductant	Reduction conditions: GO : H_2O ratio	GO : reductant ratio	Mixing time (h)	Temp (°C)	Reaction time (h)	Comment	Ref.
$[CH_2CH(OH)]_n$, $NaBH_4$, NaOH	5 : 1	50 : 7	0.75	90	4	NaOH (0.1 M) was slowly added to adjust pH to 11. Combination of 3 reductants and thermal treatment. Transmission electron micrographs showed darker regions and wrinkles (induced folding and re-stacking of layers at the edges)	63

to develop novel materials. An example of useful class composites is those in which RGO is applied as a metal catalyst support owing to the large surface area, chemical stability and thermal stability of RGO, and synergistic effect of components.[96,97]

The GO reduction protocol with respect to the RGO is critical to potential applications of the material. For example, Lee *et al.*[108] established that the microwave assisted reduction (resulting in *d*-spacing of 0.39 nm) was more appropriate in accelerating the transport of lithium ions relative to the NH_2NH_2 reduced GO (culminating in *d*-spacing of 0.37 nm) for their lithium-ion battery application work (Table 4). The investigation of reduction protocols against specific applications is scarce in the recent literature (Tables 3–5) despite the lucrative potential in this research direction.

3.3 Review of recent reduction methods

The initial requirement was to achieve the most reductive state, closer to that of graphene but well exfoliated. However, this has evolved to the need to achieve reduction alongside physicochemical property tailoring for specific needs. This means the current thrust is not just achieve a material with characteristics closer to those of graphene, but also to develop functional materials and establish a better understanding of the nanostructural parameters. This shift is crucial towards reproducibility of the RGO-based materials and the upscaling goals. Both the parent GO (synthesis method) and reduction conditions are key in tailoring the properties of RGO.[8,18] The wide-ranging precursors for GO and reduction protocols have generated vast amounts of variations between the RGO materials reported to date and this is a current challenge in standardisation. The oxygen-containing functionalities of GO are removed by three main approaches to RGO, namely, thermal,[36,109] electrochemical[110] and chemical methods, and a combination of methods.[111,112] For illustration, Regis *et al.*[112] employed a combination of ascorbic acid and near-ultraviolet light to enhance the reduction rate of GO (Table 3). An extremely high C/O ratio (>246) was reported from a combination of $NaBH_4$ and thermal treatment at 1100 °C procedures.[8] The reduction driving force for the thermal, electrochemical and chemical methodologies is temperature, electrical current and chemical potential, respectively, therefore, RGO materials of different characteristics are obtained.[2] Distinct physicochemical properties of RGO are generated by the synthesis protocols followed.[113] For example, reflux of GO in 2% aqueous green tea extract produced RGO with a large surface area (Table 3).[114]

3.3.1 Biologically derived chemical approach. Among these methodologies, the simplicity (also using simple equipment) and cost-effectiveness have placed the biologically derived chemical approach in good standing for large-scale production. In a drive for furthering the advantages of this method, several reductants derived from renewable biological sources, such as, ascorbic acid,[19,115] Azadirachta indica extract,[116] *atriplex halimus* leaves extract,[117] *clinacanthus nutans* (leaf extract),[118] *Cetraria islandica* ach. extract,[6] *eclipta prostrata* (phytoextract),[56] *Leucas aspera* (Thumbe, a leaves extract),[119] terpenoids and polyphenols (*vernonia amygdalina* extract),[35] *Chenopodium album* (vegetable extract),[120] olea europaea (olive extract),[121] *Murraya koenigii* (leaf extract),[122] and green tea extract,[114,123–125] have been reported for RGO synthesis (Table 3).

The reducing and stabilizing effect of most plant extracts are due to their OH^- and C=O moieties.[125] Ascorbic acid ($C_6H_8O_6$) is mild, non-flammable, functions as a reductant in acidic as well as alkaline pH and has nontoxicity advantageous (no gaseous by-products) over other chemical reductants.[5,103,126] $C_6H_8O_6$ is a competing alternative to hydrazine hydrate due to ability to attain similar C/O ratios, its abundance and antioxidative traits. Whilst reduction is possible at room temperature, the reviewed recent articles suggest that the use of $C_6H_8O_6$ as a reductant requires a mild heating of ~95 °C (Table 3). The mild heating is necessary for achieving appreciable reduction in a short time and despite this, the low temperature requirements still qualify the use of $C_6H_8O_6$ reductants as a green approach. Other reduction conditions in combination with ascorbic acid, such as stirring (rate and mode), high GO : reductant ratio, sonication, and alkaline pH, also shorten the reaction time from 48 to ~1 h.[112]

The use of biologically derived reductants is an interesting progress towards the sustainability of graphene-based materials, since both GO and RGO can also be biologically derived.[127–129] This is a step near the elimination of expensive, explosive, toxic and carcinogenic chemicals;[122,124] such as hydrazine (and its derivatives),[43,58] and sodium borohydride;[130] that harm the environment. This is a highlight of the tremendous potential of biologically derived reductants not only due to

Table 4 Thermal synthesis methods for RGO

	Reduction conditions						
Reduction method/reductant	Gas	GO : reductant ratio	Mixing time (h)	Temp (°C)	Reaction time (h)	Comment	Ref.
Thermal	Ar	—	—	300	—	The *d*-spacing decreased from 0.79 to 0.43 nm after reduction	57
Thermal	Ar	—		350	1	The method used a tube furnace and an inert atmosphere	146
Thermal	Ar	—	—	400		The Ar flow rate was 0.1 L min^{-1} and the heating rate was 10 °C min^{-1}. Temperatures of 250, 300 and 400 °C attained increased C/O ratios of 6.13, 6.16 and 6.46 from 2.41 of GO	33
Thermal	Air	—	—	50	168	The notable significance of this work was the ability to thermally reduce GO at a low temperature of 50 °C. The XRD peak $2\theta \sim 24°$ was a signal of reduction	144
Thermal	Air/He	—	—	500	—	Air flow rate at 300 °C (ramped at 30 °C min^{-1}) then He at 10 °C min^{-1} between 300 and 500 °C. A large surface area of 439 m^2 g^{-1} attained	147
Thermal	N_2–H_2	—	—	400	1	N_2–H_2 flow rate was 80/40 sccm and heating rate was 10 °C min^{-1}. No direct determination of reduction effect	148
Thermal/CH_4N_2S	N_2	15 : 38	∼12	800	2	Ramping rate of 5 °C min^{-1} and reduction simultaneously done with N-doping (∼10 at%)	100
Thermal/CH_3CH_2OH, NH_3	—	—	24	1200	2	The drying was carried out at 100 °C for 24 h before thermal reduction, π–π* peak shifted from 229 nm to 254 nm	98
Thermal/CH_3CH_2OH	—	—	24	1000	0.03	CH_3CH_2OH (70%) was mixed by ultrasonic treatment before and after thermal treatment for 24 and 3 h, respectively, to aid exfoliation and minimise the often-enumerated agglomeration of RGO sheets	68
Reflux/L-Methionine	—	—	—	80	12	L-methionine has a reducing effect on GO	149
Spray pyrolysis	Air	—	—	150		Spraying setup: airbrush nozzle (aperture size – 0.4 mm) and air compressor at 4 bars. The method is based on the thermal decomposition, which facilitates reduction	36
Pulsed laser	N_2	—	—	—	—	Nd:YAG laser source ($\lambda = 266$ nm, $\nu = 10$ Hz), evacuated to 10–2 Pa before filling reaction chamber with N_2 at 20 Pa. The π–π* peak indicated restoration aromaticity	150
Ultraviolet laser	—	—	—	50	96	Sample put in an ultraviolet chamber then irradiated with a Phillips F5-40 lamp at an intensity of 12.4 W m^{-2} and wavelength range of 300–320 nm. Resistance decreased from 7.05 × 10^3 (for GO) to 4.45 × 10^3 and 1.27 × 10^3 Ω after treatment for 48 and 96 h, respectively	151

Table 4 (*Contd.*)

	Reduction conditions						
Reduction method/reductant	Gas	GO : reductant ratio	Mixing time (h)	Temp (°C)	Reaction time (h)	Comment	Ref.
Hydrothermal and thermal	Ar	—	4	900°	2	GO was initially treated at 100 °C for 1 h, then kept at 180 °C for 3 h before cooling to room temperature, filtering, terminating with H_2O_2, neutralisation to pH 7 and final treatment. The approach was different from the usual protocol of oxidation, termination, purification, and reduction, allowed H_2SO_4 recycling and simplified purification *via* filtration	152
Hydrothermal and thermal/2-chloroethylamine hydrochloride	—	3 : 20	4	500	3	Hydrothermal treatment performed before the thermal step for 12 h at 180 °C (rate: 10 °C min^{-1}). Thermal treatment was in two steps: at 200 °C for 1 h (5 °C min^{-1}) then at 500 °C for 3 h. XRD peaks at $2\theta \sim 26°$ (002) and ~44° (100) ascribed to graphite and hexagonal structure of graphite planes	153
Thermal and hydrothermal/H_3BO_3, CH_4N_2S, $C_2H_8N_2$	Ar	1 : 20	1	900	5	CH_4N_2S (4 mol) and $C_2H_8N_2$ (4 mL) were added prior to hydrothermal treatment at 200 °C for 12 h. Method was sequential doping to avoid formation of B–N bonds that may cause lowered activity of the target catalyst	154

	Reduction conditions						
Reduction method/reductant	GO : H_2O ratio	GO : reductant ratio	Mixing time (h)	Temp (°C)	Reaction time (h)	Comment	Ref.
Hydrothermal	1 : 2	—	0.5	160	3	Broad XRD peaks at $2\theta \sim 24°$ (002) and 43° (102), and UV-vis absorption maxima shift from 232 to 275 nm were signature peaks for RGO	155
Hydrothermal	1 : 4	—	2	180	27	Stirring was at 500 rpm and unlike most hydrothermal treatments, beaker with silicon oil was use for heating. Reaction time was long and reduction was signalled by the disappearance of the sharp C–O peak at 1067 cm^{-1}	60
Hydrothermal	—	—	—	120	4	Method lacked direct assessment of reduction effect. Decrease in defect intensity upon reduction is a possibility, but not always, and implication of effective reduction	106
Hydrothermal	—	—	—	150	6	The amount of water added was not provided	156
Hydrothermal/NaOH	2 : 1	—	1.67	200	24	The NaOH was used to adjust pH to ~10. Reduction confirmed by FTIR spectrum that showed two unique peaks at 1565 and 1193 cm^{-1}	157

Table 4 (*Contd.*)

Reduction method/reductant	Reduction conditions: GO : H_2O ratio	GO : reductant ratio	Mixing time (h)	Temp (°C)	Reaction time (h)	Comment	Ref.
Hydrothermal/ CH_4N_2S	1 : 1	15 : 28	1.67	180	12	Mixing was done by means of ultrasonic treatment at 750 W and 20 kHz after dispersing GO in H_2O by stirring for 0.5 h	158
Hydrothermal/ $(CH_2)_3CH_2O$	—	12 : 1	0.3	130	8	Ultrasonic treatment was attributed to both GO exfoliation and the carboxylic acid-carboxylate ion moiety transformations. The C/O ratio decreased from 2.39 to 1.63	159
Hydrothermal/NaOH	16 000 : 7	—	0.5	180	12	Uncoordinated oxygen moieties were removed	160
Hydrothermal	2 : 1	—	—	180	12	Reduction generated the most stable composites with F-carbon nanofiber (the highest negative zeta potential of −45 mV)	161
Hydrothermal	—	—	—	180	8	The reduction reaction induced π–π stacking	162
Hydrothermal/ $H_2NCH_2CH_2NH_2$	1 : 2		1.15	120	12	Details of the amount of $H_2NCH_2CH_2NH_2$ were not provided	163
Hydrothermal/NaOH	—	20 : 1	1.17	200	4	The disappearance of the C–H bonding, and declined intensities of the O–H (at 3324 cm^{-1}) and C=O bending peaks (at 1812 cm^{-1}) were the signatures of the formation of RGO	84
Hydrothermal	—	—	—	300	24	Fluorination was done after reduction by introducing F_2–N_2 (1 : 5) and removal unbound fluorine was carried out by washing with dilute Na_2CO_3 and H_2O	164
Hydrothermal	10 : 1	—	0.33	200	24	The π–π* transition of the conjugated C=C bonding was redshifted to 270 nm	64
Hydrothermal/ NH_2NH_2	—	—	—	200	0.33	The first treatment was at 95 °C for 2 h and then the second at 200 °C in NH_2NH_2 (0.2 M). RGO floated on the H_2O surface and the Raman I_D/I_G increased from 1.05 to 1.33 after reduction due to the elimination of oxygen moieties and the formation of defects along with the recovery π-system	165

Reduction method/ reductant	Reduction conditions: GO : solvent ratio	GO : reductant ratio	Mixing time (h)	Temp (°C)	Reaction time (h)	Comment	Ref.
Solvothermal/Green tea extract	—	1 : 1	—	90	8	The stirring was continuous at 200 rpm during the reaction. Absence of the GO typical peak at $2\theta \sim 10°$ confirmed complete reduction	123
Solvothermal/*Murraya koenigii*	—	—	0.67	100	12	The extract was rich in polyphenol and reduction was also ascribed to this chemical	122

Table 4 (*Contd.*)

	Reduction conditions						
Reduction method/ reductant	GO : solvent ratio	GO : reductant ratio	Mixing time (h)	Temp (°C)	Reaction time (h)	Comment	Ref.
Solvothermal/ CH_2OHCH_2OH	5 : 3	20 : 1	2.5	200	8	The UV-vis $\pi \rightarrow \pi^*$ peak at ~270 nm was used to confirm reduction and restoration of aromatic C=C bonds	75
Solvothermal/ $C_2H_4(NH_2)_2$/ CH_2OHCH_2OH	15 : 1	~1 : 1	0.5	180	10	Thermal treatment in two reductants achieved reduction. The peak at $2\theta \sim 26°$ (002) plane was a signal for GO reduction	59
Solvothermal/H_2/ $(CH_3)_2NC(O)H$/ $HOCH_2(CH_2)_2O$	1 : 6	5 : 6	1	180	8	The dropwise addition of NH_4OH adjusted the pH to >10. Hydrothermal treatment done in N_2 (at 0, 5, and 10 bar) and Ar (85%)–H_2 (15%) atmosphere. The injection of H_2 improved crystallinity of RGO.	166
Solvothermal/$C_2H_8N_2$	—		—	120	12	$C_2H_8N_2$ was a source of N_2 as well as an additional reductant	167
Solvothermal	2 : 5	—	1	140	12	Nitrates are well known as oxidants; hence, minimal reduction despite thermal treatment	168
Solvothermal/$NH_{3(aq)}$	—	1 : 10	—	160	8	Reduction and N-doping achieved with low temperature and indicator was increase in the XPS C/O ratio from 2.48 (GO) to 11.36	71
Solvothermal/ $CH_2(C_6H_4NH_2)$/ CH_3CH_2OH/NaOH	—	15 : 1	1	180	10	NaOH (0.1 M) adjusted pH to 10. Disappearing of FTIR oxygen peaks and observed weak C–H stretching vibration (2915–2935 cm^{-1}) of the aliphatic CH_2 moiety	169
Solvothermal/ $N_2H_4 \cdot H_2O/NH_3$	3 : 25		1.5	180	12	$H[OCH_2CH_2]_nOH$ was the solvent. $N_2H_4 \cdot H_2O$ and H_2O was used to keep pH at 11. Combination-treatment induced pyrrolic-, pyridinic-, oxidized- and graphitic-N	170
Solvothermal-microwave irradiation	—	—	2	120	0.5	Solvent: C_4H_9NO (DMF). The reduction was signalled by UV-vis absorption maxima at 265 nm (π–π^* transitions of aromatic C=C) and an increase in C/O ratio from 0.61 to 2.52	3
Microwave-assisted solvothermal	413 : 180	—	0.5	—	0.19	Solvent: C_5H_9NO Treatment was in an Anton-Paar Microwave (power/time ratios: 600 W/0.19 h) (most effective), 800 W/ 0.14 h, and 1000 W/0.117 h (fastest)	2
Microwave-assisted solvothermal/$C_2H_6O_2$	—	—	—	180	0.1	XRD spectrum (002) plane was an indicator of reduction	171
Microwave-assisted hydrothermal/NH_3	—	—	8	150	0.08	NH_3 used to adjust pH to 10. Simultaneous microwave rapid reduction and N-doping (NH_3 was N_2 source)	172
Microwave-assisted hydrothermal	—			150	0.25	Microwave irradiation was at 400 W. Raised intensity peaks of the C–C and C=C signalled the reduction process	26

Table 4 (*Contd.*)

Reduction method/ reductant	Reduction conditions: GO : solvent ratio	GO : reductant ratio	Mixing time (h)	Temp (°C)	Reaction time (h)	Comment	Ref.
Microwave-assisted hydrothermal/$NH_{3(aq)}$	—	—	2	180	0.33	NH_3 (6%) was added dropwise to achieve a pH of 10. The $NH_{3(aq)}$ support the reduction of GO.	173

Reduction method/ reductant	Reduction condition: GO : H_2O	GO : reductant ratio	Mixing time (h)	Power (W)	Reaction time (h)	Comment	Ref.
Microwave	—	—	—	700	0.08	Quick method	174
Microwave/NH_3	5 : 1	500 : 1	0.67	500	0.025	The peak of the XRD spectrum at $2\theta = 26.4°$ was broad and a signal for reduction	24
Microwave/CH_4N_2S	—	—		700	0.17	Microwave frequency was 2.45 GHz. The 2θ peak ~26° (002) plane was a reduction indicator	175
Microwave	—	—	—	—	0.17	The first treatment for 0.17 h was in DMF and then in toluene for 0.083 h to complete the reduction. The wider (002) XRD peak ($2\theta = 23°$) with a *d*-spacing 0.39 nm was reduction indicator	108
Microwave and thermal/$NH_{3(aq)}$	~1 : 1	—	2	—	0.17	Freshly prepared $NH_{3(aq)}$ was added to maintain pH at 7. Reduction was confirmed by a broad XRD peak at $2\theta = 24°$ assigned to the (002) plane	176
Gamma irradiation/ CH_3CH_2OH	—	1 : 1	0.5	—	—	Irradiation was done with 100 kGy of γ-ray at 2 kGy h^{-1} from a ^{60}Co source. The γ-rays generates reductive radical ($H^{\bullet}$) that reduces GO and *d*-spacing of 38.6 nm	177
Gamma irradiation/ $CH_3CH(OH)CH_3$	—	—	—	—	—	N_2 was bubbled prior to irradiation with an absorbed dose of 75 kGy at 4.5 kGy h^{-1} from a ^{60}Co source under the ambient conditions. $CH_3CH(OH)CH_3$ was an $^{\bullet}OH^-$ scavenger and forms reactive radicals that were excellent reductants	178
Plasma-assisted/ $CO(NH_2)_2$	—	2 : 25	12	200	0.25	Radio frequency inductively coupled plasma (13.56 MHz, pressure: 15 Pa, H_2 flow rate: 15 sccm) was used to simultaneously reduce and N-dope (N_2 source: $(CO(NH_2)_2)$)	66

their biocompatibility nature, but also because the approach is a suitable standardisation step in future research.

3.3.2 Inorganic chemical approach. Despite these environmental limitations and also the introduction of impurities such as N moieties, hydrazine monohydrate ($NH_2NH_2 \cdot H_2O$) is still commonly used as a reductant for aqua GO due to its high efficacy and weak reactivity with water unlike most chemical reductants (Table 3).[12,112]

In general, most chemical reduction methodologies initially involve the dispersion of GO in water through ultrasonic treatment (Table 3). A common feature of the recent chemical reduction methodologies is the use of mild heating in the 80–100 °C range. This could be a decent basis for developing standardised reduction protocols that will ease comparison between methods in terms of efficacy and reproducibility. For uniformity, the GO : reductant ratios presented in Table 3 were

calculated using the main reductant (where more than one possible reductant was used) assuming the density of water was 1 g cm^{-3}. According to the reviewed works, the calculated GO : reductant ratios are arbitrary; hence, the recent chemical reduction protocols are difficult to compare in terms of efficacy (Table 3). Economic and environmental sustainability considerations are a conceivable fair stimulation to focusing more on lower GO : reductant ratios, particularly in the case of inorganic reductants, in future research.

A few of these reports presented further issues with the missing pertinent details about the amount of reductant that was used. However, satisfactory qualitative tests for RGO formation were present in most reports. More insights towards a standardised GO : reductant ratio is needed in future research to aid the progression to commercialisation of products.

Future research directions must seek a better understanding of chemical reduction mechanisms, eliminate the use of toxic chemicals, and shift towards green chemistry principles *via* the use of biologically derived reductants with comparable reduction efficacies and avoid inorganic reducing agents. This approach has positive prospects as a strategic value-addition exercise for agricultural waste, since high tonnage is produced globally each year. Most chemical reduction protocols involve purification steps that are not only monotonous, but also add substantial costs to material development at large-scale. The purification procedures often involve washing and neutralisation steps with deionised/ultra-pure water to remove excess chemical reductants, centrifuging and drying for ~24 h.[112,117,119,121,126,128,131] Careful and cost-effective removal of residual reductants must be sought in future research to avoid chemical contaminants that may negatively affect RGO quality and intended applications. Another drawback of chemical reductants is their selective elimination of oxygen moieties.[19,30] Despite the shortfalls, chemical reduction methods have the advantage of short purification times and low energy requirements when compared to other methods; therefore, they are better suited for the principles of green chemistry and sustainability.

3.3.3 Thermal approach. Thermal reduction varies according to the heat sources, setups and conditions, such as gas atmospheres, solvent systems, temperatures, and duration. The recent reduction examples are inclusive of laser, gamma rays, microwave, hydrothermal, solvothermal, plasma, reflux and simple heating setups (ordinarily referred to as thermal) (Table 4). This is another feasible source of discrepancies in the physicochemical characteristics of the reported RGO materials.

Thermal reduction of GO has been reported at temperatures as low as 50 °C, however, the reaction time was one of the longest reported, that is, 1 week (Table 4).[144] This suggests that a potential setback to progression can be avoided in future works through careful calculations that balance reaction time and temperature inputs, since the random lowering of one parameter could sum up to the same energy requirements. Despite achievable reduction at low temperatures that mostly remove labile oxygen groups, Coros *et al.*[33] established that reduction increases with temperature (Table 4). This is possibly needed to meet the energy requirements for breaking chemically stable bonds in oxygen moieties under an inert environment.

However, high thermal temperatures can generate extremely toxic volatile organic hydrocarbons.[58] Exfoliation through thermal means is facilitated by the evolution of gases (such as CO_2 from the decomposition of oxygen moieties and H_2O) and weight loss (~30%) creates vacancies and topological defects.[12,31,68] Despite the minimal contamination issues, relative to chemical means, the drawbacks that may be associated with thermal methods include the requirement of higher temperatures (mainly 400–1000 °C)[30] for effective reductions and the possible build-up of explosive gas evolutions (Table 4).

Hydrothermal and solvothermal reduction of GO refers to chemical transformations that result in the removal of oxygen moieties in a supercritical environment of water and specified solvents, respectively, triggered by heating.[145] Hydrothermal and solvothermal treatments can be viewed as stratagems that lower the temperature required for the reduction of GO by utilising high pressures and surface chemistry. Therefore, the hydrothermal and solvothermal reduction temperatures and durations in the recent reviewed reports were mostly in the 160–200 °C and 8–12 h ranges, respectively (Table 4). This is a direction towards ease comparison between methods and reproducibility of RGO. However, lack of ratio details in most studies may hinder this advancement. The GO : H_2O ratio was commonly 1 : 2 or 2 : 1 for hydrothermal methods, while in solvothermal methods, the GO : solvent ratio was random (density of H_2O was assumed to be 1 g cm^{-3} for the calculation of GO : H_2O ratio in the Table 4).

The GO : solvent ratio in hydrothermal and solvothermal protocols still needs more work to enable comparison between solvents at given temperatures and to establish if the water/solvent should be in excess. Similarly, to the general thermal protocols, common products of both solvothermal and hydrothermal approach are CO_2 and CO gases. However, the use of lower temperatures in both solvothermal and hydrothermal methods has a lower reduction efficacy compared to thermal means. The use of organic solvents in solvothermal reduction reduces energy requirements and has better capabilities to self-generate pressure relative to hydrothermal needs.[30] Hence, future research could prudently use solvothermal methods, however, water as a solvent still offers affordability and safe handling advantages.

Microwave reduction of GO is possible on an industrial scale and achieves reduction at lower energy costs relative to thermal treatment (Table 4); however, reduction efficacy is low.[23] Hence, microwave-assisted thermal reduction of GO is a strategy to accelerate thermal reduction since energy is transferred directly to reagents.[2,145,173] In this method, reduction is triggered by both heating effect, and differences in the dielectric constants of GO and the solvent, which induces an instant increase in internal temperature, consequently, causing reduction.[2,145,179] Hence, selection of an appropriate solvent system for the microwave reduction of GO is critical in this regard. An ideal solvent is one that facilitates stable GO dispersions without functionalisation of the ultimate RGO, with a high boiling point and high dielectric properties (better ability to absorb and convert

microwaves into heat energy), as well as surface tension values between 40 and 50 mJ m^{-2}.[3,179–182]

In addition, a study by Martins *et al.*[2] has hinted at the need of establishing a suitable compromise between high reduction rate and efficacy, since they are often achievable through high- and low-power inputs, respectively (Table 4). The microwave technique can also be combined with other reduction protocols. For illustration, microwave-assisted hydrothermal methods are advantageous than either microwave or hydrothermal approaches in that the combination accelerates heating, effects a more sensitive reaction, and facilitates uniform heating.[173]

The γ-irradiation has also been reported recently as a facile, green, cost-effective method for RGO production (Table 4).[177] In the presence of water or alcohol, γ-rays create $H^{\cdot}$ (reductive) and $OH^{\cdot}$ species (oxidative) due to water radiolysis. The role of alcohol is scavenging for oxidative radicals in order to stop additional oxidation of GO. The advantages of reduction by means of γ-irradiation over chemical means are the lower agglomeration in the RGO produced[177] and the absence of contamination issues. The combination of thermal treatment with chemical reductants has gained momentum in recent times towards achieving RGO with characteristics closer to that of graphene (Table 4). Despite the general calls to utilise clean chemicals in order to preserve the environment, catastrophic toxic chemicals, such as NH_2NH_2, are still being used in combination with thermal treatment (Table 4). Therefore, as a future research direction, chemical selection should be inclined to only "greener" chemicals.

The reviewed literature has also shown the combinations of methods such as chemical reduction and thermal reduction in one step (solvothermal protocols that use a solvent with reducing effects, Table 4). For example, reduction was achieved through a combination of microwave irradiation and the solvothermal protocol without the use of a chemical reductant (Table 4).[3] Thermal treatment can also be used in combination with alcohol to enhance reduction of GO (Table 4). Alcohols are relatively mild reductants due to the preservation of edge morphology.[21]

3.3.4 Electrochemical and ball milling methods. Other less popular protocols include ball milling and electrochemical reduction methods (Table 5). For illustration, a one-step electrochemical reduction of an aqueous colloidal GO suspension was done by means of linear sweep voltammetry, cyclic voltammetry and constant potential mode in the presence of a buffer electrolyte.[110] One of the acceptable proposals is that reduction occurs when GO which is located adjacent to the electrode accepts electrons and gets deposited on the electrode surface.[110]

On the other hand, in the two-step electrochemical reduction, GO is first deposited onto the electrode surface (and attachments are possibly through van der Waals forces), then dried before electrochemical reduction. When compared to chemical means, the electrochemical reduction is faster, greener, and economically more advantageous as a future research realisation.

4 Challenges and prospects

From the reviewed works it is critical to realise that RGO is a nonstoichiometric derivative of GO since numerous ratios of carbon, hydrogen, and oxygen have been reported to date.[8,32] This poses some fundamental issues in determining reproducibility of RGO by comparing atomic ratios on the basis of mass ratios per sample. The atomic ratios in RGO are influenced by synthesis methodologies which are currently wide-ranging. In addition, the precise chemical structure of GO and RGO remains obscure and still requires further modelling. The gaps in understanding RGO are due to numerous variables in oxidation methods (precursors) that lead to sample-to-sample physicochemical variations, nonstoichiometric atomic composition and unavailability of specific physicochemical characterization techniques.[12] The other drawbacks associated with full utilisation of RGO are emanating from lack of

Table 5 Electrochemical and ball milling synthesis methods for RGO

Reagents other than GO	Reduction conditions	Remark	Ref.
H_2 (reductant)	Ball milling: H_2 environment for 8 h, with purging every 2 h, during dual-drive ball milling of 30 Hz	The C/O ratio of the RGO was 17.51 and the method was eco-friendly and versatile	183
H_2SO_4	Electrochemical: graphite foils (1 cm apart) were electrodes in H_2SO_4 (0.5 M). A +4 V was the applied anodic potential at room temperature	Partial oxidation of graphene is formed through formation of radicals such as, OH^- radicals	184
PTFE, KOH (reductant)	Electrochemical: GO (50 mg) was added to the paraffin oil to form a paste, then ultrasonicated at 100 W and room temperature for 0.5 h. Subsequently, this was filled into a PTFE tube prior to electrochemical treatment of −1.2 to 0 V with a scan rate of 100 mV s^{-1} in a cell with KOH (0.1 M, pH = 12.0)	Reduction was confirmed by a diffraction peak at $2\theta \sim 25°$ and weak peak at about 42°	185

standardised methodologies for reducing GO, *i.e.*, lack of pertinent details such as reduction time, GO : reductant ratios, and use of arbitrary ratios is challenging reproducibility and adoption of methods at industrial scale.

The common use of X-ray diffraction and ultra-violet visible spectroscopies as signature techniques for confirming the formation of RGO in most recent reports is a step in the standardisation direction. Future research may also utilise the scarcely used C/O ratio from X-ray photoelectron spectroscopy, since this can enable easy comparison between methods and determination of reproducibility. With what has been reported to date, RGO may be referred to as a family of materials and not as a single composition since current proposed structures differ according to varied oxidation conditions (in each of the reported methods) and properties of starting materials.[16,35] The limited understanding of the chemical structure of GO could be a major setback in understanding RGO (which is simply a derivative of GO). In addition, lack of large-scale and cost-effective production of RGO at the present time is a drawback to progression towards commercialisation despite the highlighted potentials through physicochemical properties and recent applications. Hence, this in turn is limiting breakthroughs in various potential large-scale industrial applications. In-depth understanding of reduction mechanisms, elimination of toxic reductants and the use of low temperatures (for energy-saving purposes), design of simple reduction procedures, and more studies of biologically derived reductants are critical and potentially sustainable steps as future research directions. This trajectory is promising in driving RGO towards its full potential in order to broaden and/or further advance related properties. The reviewed work highlights RGO as a potential and strategic material for achieving sustainable, environmentally friendly, low-cost, high-performing, and large-scale production and use in functional devices and/or processes to pave the way for commercialisation. This can drive future commercial viability aspects of RGO as a material.

Author contributions

ETM and EM designed the work, investigated the literature, wrote the original draft, assembled the figures and tables, and revised the manuscript.

Conflicts of interest

The authors report that there are no competing interests to declare.

Acknowledgements

This work was supported by the University of Zimbabwe and Bindura University of Science Education.

References

1 A. D. Sontakke and M. K. Purkait, *Chem. Eng. J.*, 2021, **420**, 129914.
2 A. L. B. S. Martins, E. F. da Silva, M. F. V. Marques and W. A. Pinheiro, *Mater. Res.*, 2022, **25**, e20220140.
3 R. Tarcan, M. Handrea-Dragan, O. Todor-Boer, I. Petrovai, C. Farcau, M. Rusu, A. Vulpoi, M. Todea, S. Astilean and I. Botiz, *Synth. Met.*, 2020, **269**, 116576.
4 E. T. Mombeshora and A. Stark, *Biomass Convers. Biorefin.*, 2023, **13**, 4619–4638.
5 N. M. Dat, P. N. B. Long, D. C. U. Nhi, N. N. Minh, L. M. Duy, L. N. Quan, H. M. Nam, M. T. Phong and N. H. Hieu, *Synth. Met.*, 2020, **260**, 116260.
6 Z. Çıplak, B. Getiren, C. Gökalp, A. Yıldız and N. Yıldız, *Chem. Eng. Commun.*, 2019, **207**, 559–573.
7 F. Farjadian, S. Abbaspour, M. A. A. Sadatlu, S. Mirkiani, A. Ghasemi, M. Hoseini-Ghahfarokhi, N. Mozaffari, M. Karimi and M. R. Hamblin, *ChemistrySelect*, 2020, **5**, 10200–10219.
8 S. Mao, H. Pu and J. Chen, *RSC Adv.*, 2012, **2**, 2643.
9 R. Tarcan, O. Todor-Boer, I. Petrovai, C. Leordean, S. Astilean and I. Botiz, *J. Mater. Chem. C*, 2020, **8**, 1198–1224.
10 D. W. Lee, L. V. De Los Santos, J. W. Seo, L. L. Felix, A. D. Bustamante, J. M. Cole and C. H. W. Barnes, *J. Phys. Chem. B*, 2010, **114**, 5723–5728.
11 S. N. a. Y. Matsuo, *Carbon*, 1994, **32**, 469–475.
12 D. R. Dreyer, S. Park, C. W. Bielawski and R. S. Ruoff, *Chem. Soc. Rev.*, 2010, **39**, 228–240.
13 Y. X. Li, C. Y. Sun, C. J. Yu, C. X. Wang, Y. J. Liu and Y. B. Song, *Adv. Mater. Res.*, 2012, **476–478**, 1488–1495.
14 D. R. Dreyer, A. D. Todd and C. W. Bielawski, *Chem. Soc. Rev.*, 2014, **43**, 5288–5301.
15 A. Lerf, H. He, M. Forster and J. Klinowski, *J. Phys. Chem. B*, 1998, **102**, 4477–4482.
16 T. Szabó, O. Berkesi, P. Forgó, K. Josepovits, Y. Sanakis, D. Petridis and I. Dékány, *Chem. Mater.*, 2006, **18**, 2740–2749.
17 E. Aliyev, V. Filiz, M. M. Khan, Y. J. Lee, C. Abetz and V. Abetz, *Nanomaterials*, 2019, **9**, 1180.
18 P. P. Brisebois and M. Siaj, *J. Mater. Chem. C*, 2020, **8**, 1517–1547.
19 E. T. Mombeshora, P. G. Ndungu and V. O. Nyamori, *Electrochim. Acta*, 2017, **258**, 467–476.
20 E. T. Mombeshora and A. Stark, *Mater. Chem. Phys.*, 2022, **277**, 125535.
21 W. Yu, L. Sisi, Y. Haiyan and L. Jie, *RSC Adv.*, 2020, **10**, 15328–15345.
22 R. Ikram, B. M. Jan and W. Ahmad, *J. Mater. Res. Technol.*, 2020, **9**, 11587–11610.
23 L. Dong, J. Yang, M. Chhowalla and K. P. Loh, *Chem. Soc. Rev.*, 2017, **46**, 7306–7316.
24 R. Kumar, S. M. Youssry, M. M. Abdel-Galeil and A. Matsuda, *J. Mater. Sci.: Mater. Electron.*, 2020, **31**, 15456–15465.
25 A. C. Lazanas, A. Katsouras, M. Spanos, G. M. Manesi, I. Moutsios, D. V. Vashurkin, D. Moschovas, C. Gioti, M. A. Karakassides, V. G. Gregoriou, D. A. Ivanov, C. L. Chochos and A. Avgeropoulos, *Polymers*, 2022, **14**, 5292.

26 S. Jangu, B. K. Satpathy, M. Raju, C. Jacob and D. Pradhan, *Dalton Trans.*, 2021, **50**, 6878–6888.
27 M. J. Yoo and H. B. Park, *Carbon*, 2019, **141**, 515–522.
28 E. T. Mombeshora, P. G. Ndungu and V. O. Nyamori, *New Carbon Mater.*, 2017, **32**, 174–187.
29 T. Nakajima, A. Mabuchi and R. Hagiwara, *Carbon*, 1988, **26**, 357–361.
30 R. Singh, S. Ullah, N. Rao, M. Singh, I. Patra, D. A. Darko, C. P. J. Issac, K. Esmaeilzadeh-Salestani, R. Kanaoujiya and V. Vijayan, *J. Nanomater.*, 2022, **2022**, 8731429.
31 C. Kavitha, *Mater. Today: Proc.*, 2022, **49**, 811–816.
32 L. Sun, *Chin. J. Chem. Eng.*, 2019, **27**, 2251–2260.
33 M. Coros, F. Pogacean, A. Turza, M. Dan, C. Berghian-Grosan, I.-O. Pana and S. Pruneanu, *Phys. E*, 2020, **119**, 113971.
34 T. F. Emiru and D. W. Ayele, *Egypt. J. Basic Appl. Sci.*, 2017, **4**, 74–79.
35 B. Meka Chufa, B. Abdisa Gonfa, T. Yohannes Anshebo, G. Adam Workneh and D.-R. Hang, *Adv. Condens. Matter Phys.*, 2021, **2021**, 6681710.
36 A. S. AlShammari, M. M. Halim, F. K. Yam and N. H. M. Kaus, *Mater. Sci. Semicond. Process.*, 2020, **116**, 105140.
37 A. Adetayo and D. Runsewe, *Open J. Compos. Mater.*, 2019, **09**, 207–229.
38 H. Altaee and H. A. Alshamsi, *J. Phys.: Conf. Ser.*, 2020, **1664**, 012074.
39 I. Bargaoui, N. Bitri and J. M. Menard, *ACS Omega*, 2022, **7**, 11973–11979.
40 C. Hao, T. Gao, A. Yuan and J. Xu, *Chin. Chem. Lett.*, 2021, **32**, 113–118.
41 N. Maslekar, R. A. Mat Noor, R. P. Kuchel, Y. Yao, P. B. Zetterlund and V. Agarwal, *Nanoscale Adv.*, 2020, **2**, 4702–4712.
42 K. Ahmad, M. A. Shinde and H. Kim, *Microchem. J.*, 2021, **169**, 106583.
43 M. Ebrahimi Naghani, M. Neghabi, M. Zadsar and H. Abbastabar Ahangar, *Sci. Rep.*, 2023, **13**, 1496.
44 A. A. Alghyamah, S. Haider, U. Khalil, R. Khan, A. Haider, W. A. Almasry, R. Ihsan, P. Tahira, I. Wazeer and A. Chafidz, *Curr. Appl. Phys.*, 2022, **40**, 1–11, DOI: **10.1016/j.cap.2020.03.002**.
45 Y. Zhu, S. Murali, W. Cai, X. Li, J. W. Suk, J. R. Potts and R. S. Ruoff, *Adv. Mater.*, 2010, **22**, 3906–3924.
46 V. Kumar, T. K. Mandal, A. Kumar, M. N. Alam, N. Parvin, S. W. Joo, D. J. Lee and S.-S. Park, *eXPRESS Polym. Lett.*, 2022, **16**, 978–995.
47 N. N. Malinga and A. L. L. Jarvis, *J. Nanostruct. Chem.*, 2020, **10**, 55–68.
48 C. Monteserín, M. Blanco, E. Aranzabe, A. Aranzabe, J. M. Laza, A. Larrañaga-Varga and J. L. Vilas, *Polymers*, 2017, **9**, 449.
49 H. Sun, L. Ling, Z. Ren, S. A. Memon and F. Xing, *Nanomaterials*, 2020, **10**, 113.
50 S. Yan, P. He, D. Jia, Z. Yang, X. Duan, S. Wang and Y. Zhou, *Ceram. Int.*, 2016, **42**, 752–758.
51 Y. Zhang, Q. Zhang, D. Hou and J. Zhang, *Appl. Surf. Sci.*, 2020, **504**, 144152.
52 M. V. Kiamahalleh, A. Gholampour, D. N. H. Tran, T. Ozbakkaloglu and D. Losic, *Constr. Build. Mater.*, 2020, **250**, 118832.
53 R. A. Soler-Crespo, W. Gao, P. Xiao, X. Wei, J. T. Paci, G. Henkelman and H. D. Espinosa, *J. Phys. Chem. Lett.*, 2016, **7**, 2702–2707.
54 Y. Sun, X. Tang, H. Bao, Z. Yang and F. Ma, *RSC Adv.*, 2020, **10**, 29610–29617.
55 M. Tavakol, A. Montazeri, S. H. Aboutalebi and R. Asgari, *Appl. Surf. Sci.*, 2020, **525**, 146554.
56 R. Chuah, S. C. B. Gopinath, P. Anbu, M. N. Salimi, A. R. W. Yaakub and T. Lakshmipriya, *3 Biotech*, 2020, **10**, 364.
57 H. Ma, X. Chen, S. Mohammed, Y. Hu, J. Lu, G. P. Simon, H. Hou and H. Wang, *J. Mater. Chem. A*, 2020, **8**, 25951–25958.
58 A. Jirickova, O. Jankovsky, Z. Sofer and D. Sedmidubsky, *Materials*, 2022, **15**, 920.
59 G. Vinodhkumar, J. Wilson, S. S. R. Inbanathan, I. V. Potheher, M. Ashokkumar and A. C. Peter, *Phys. B*, 2020, **580**, 411752.
60 K. O. Olumurewa and M. A. Eleruja, *Fullerenes, Nanotubes Carbon Nanostruct.*, 2022, **30**, 913–922.
61 E. Muchuweni and E. T. Mombeshora, *Renew. Energy Focus*, 2023, **45**, 40–52.
62 E. T. Mombeshora, E. Muchuweni, M. L. Davies, B. S. Martincigh and V. O. Nyamori, *New J. Chem.*, 2023, **47**, 3502–3515.
63 A. Nisar, M. Saeed, M. Muneer, M. Usman and I. Khan, *Environ. Sci. Pollut. Res.*, 2022, **29**, 418–430.
64 M. Ikram, A. Raza, M. Imran, A. Ul-Hamid, A. Shahbaz and S. Ali, *Nanoscale Res. Lett.*, 2020, **15**, 95.
65 D. Lu, L. P. Ma, J. Zhong, J. Tong, Z. Liu, W. Ren and H. M. Cheng, *ACS Nano*, 2023, **17**, 3587–3597.
66 H. Sun, Q. Wang, T. Wu, Y. Miao and Y. Fang, *Appl. Surf. Sci.*, 2020, **527**, 146574.
67 J. H. Ji, G. Lee and J. H. Koh, *Sci. Rep.*, 2022, **12**, 15583.
68 L. G. P. Tienne, L. d. S. Candido, B. d. S. M. da Cruz, F. F. Gondim, M. P. Ribeiro, R. A. Simão, M. d. F. V. Marques and S. N. Monteiro, *J. Mater. Res. Technol.*, 2022, **18**, 4871–4893.
69 S. Rai, R. Bhujel, M. Khadka, R. L. Chetry, B. P. Swain and J. Biswas, *Mater. Today Chem.*, 2021, **20**, 100472.
70 Y. Yan, Y. Meng, H. Zhao, E. Lester, T. Wu and C. H. Pang, *Bioresour. Technol.*, 2021, **331**, 124934.
71 E. T. Mombeshora, *J. Mater. Sci.: Mater. Electron.*, 2023, **34**, 521.
72 Z. Lin, G. Waller, Y. Liu, M. Liu and C.-P. Wong, *Adv. Energy Mater.*, 2012, **2**, 884–888.
73 F. Farivar, P. Lay Yap, R. U. Karunagaran and D. Losic, *C*, 2021, **7**, 41.
74 K. Chaudhary, M. Aadil, S. Zulfiqar, S. Ullah, S. Haider, P. O. Agboola, M. F. Warsi and I. Shakir, *Fullerenes, Nanotubes Carbon Nanostruct.*, 2021, **29**, 915–928.

75 F. Soysal, Z. Çıplak, B. Getiren, C. Gökalp and N. Yıldız, *Mater. Res. Bull.*, 2020, **124**, 110763.
76 P. Tambe, *Mater. Today: Proc.*, 2022, **49**, 1294–1297.
77 J. Wu, H. Lin, D. J. Moss, K. P. Loh and B. Jia, *Nat. Rev. Chem.*, 2023, **7**, 162–183.
78 J. Wu, L. Jia, Y. Zhang, Y. Qu, B. Jia and D. J. Moss, *Adv. Mater.*, 2021, **33**, e2006415.
79 Z. Dehghani, F. Ostovari and S. Sharifi, *Optik*, 2023, **274**, 170551.
80 A. K. Gautam, M. Faraz and N. Khare, *Ceram. Int.*, 2021, **47**, 27885–27889.
81 E. T. Mombeshora, E. Muchuweni, R. Garcia-Rodriguez, M. L. Davies, V. O. Nyamori and B. S. Martincigh, *Nanoscale Adv.*, 2022, **4**, 2057–2076.
82 R. Fatima, M. F. Warsi, M. I. Sarwar, I. Shakir, P. O. Agboola, M. F. Aly Aboud and S. Zulfiqar, *Ceram. Int.*, 2021, **47**, 7642–7652.
83 D. Ranjan Rout and H. Mohan Jena, *Sep. Purif. Technol.*, 2021, **278**, 119630.
84 H. Shen, B. Jang, J. Park, H. J. Mun, H. B. Cho and Y. H. Choa, *Nanomaterials*, 2022, **12**, 2009.
85 A. M. El-Khawaga, H. Tantawy, M. A. Elsayed and A. I. A. Abd El-Mageed, *Sci. Rep.*, 2022, **12**, 17075.
86 S. O. Akpotu, I. A. Lawal, P. N. Diagboya, F. M. Mtunzi and A. E. Ofomaja, *ACS Omega*, 2022, **7**, 34054–34065.
87 H. A. A. Jamjoum, K. Umar, R. Adnan, M. R. Razali and M. N. Mohamad Ibrahim, *Front. Chem.*, 2021, **9**, 752276.
88 N. Buatong, C. Ruttanapun and C. Sriwong, *J. Taiwan Inst. Chem. Eng.*, 2023, **142**, 104667.
89 H. Zhao, J. Wang, Z. Fan, Y. Xie, D. Zhang, S. Sun, Y. Zhang and H. Cao, *Green Energy Environ.*, 2022, **7**, 440–448.
90 N. Keshmiri, P. Najmi, B. Ramezanzadeh, M. Ramezanzadeh and G. Bahlakeh, *Prog. Org. Coat.*, 2021, **159**, 106416.
91 M. H. Tran, I. Booth, B. G. daFonseca, P. Berrang, J. E. Wulff and A. G. Brolo, *ACS Omega*, 2022, **7**, 43548–43558.
92 A. Umar, A. A. Ibrahim, H. Algadi, H. Albargi, M. A. Alsairi, Y. Wang and S. Akbar, *Environ. Technol. Innovation*, 2022, **25**, 102066.
93 C. J. Brown, T. Simon, C. Cilibrasi, P. J. Lynch, R. W. Harries, A. A. Graf, M. J. Large, S. P. Ogilvie, J. P. Salvage, A. B. Dalton, G. Giamas and A. A. K. King, *J. Mater. Chem. B*, 2022, **10**, 373–383.
94 D. Verma, K. R. Ranjan, M. D. Mukherjee and P. R. Solanki, *Biosens. Bioelectron.: X*, 2022, **11**, 100217.
95 R. Niranjan, S. Zafar, B. Lochab and R. Priyadarshini, *Nanomaterials*, 2022, **12**, 191.
96 H. Chen, M. Yang, J. Yue and G. Chen, *Materials*, 2022, **15**, 8862.
97 R. Santhosh Kumar, S. Ramakrishnan, S. Prabhakaran, A. R. Kim, D. R. Kumar, D. H. Kim and D. J. Yoo, *J. Mater. Chem. A*, 2022, **10**, 1999–2011.
98 K. Singh, D. P. Barai, S. S. Chawhan, B. A. Bhanvase and V. K. Saharan, *Mater. Today Commun.*, 2021, **26**, 101986.
99 L. Cheng, C. Liu, H. Wu, H. Zhao and L. Wang, *J. Colloid Interface Sci.*, 2022, **606**, 1572–1585.
100 H. Sun, J. Li, W. Wang, Z. Wang and L. Pan, *J. Colloid Interface Sci.*, 2021, **594**, 35–46.
101 X. Tang, J.-P. Raskin, N. Kryvutsa, S. Hermans, O. Slobodian, A. N. Nazarov and M. Debliquy, *Sens. Actuators, B*, 2020, **305**, 127423.
102 S. Kazemi, M. Pourmadadi, F. Yazdian and A. Ghadami, *Int. J. Biol. Macromol.*, 2021, **186**, 554–562.
103 S. Joshi, R. Siddiqui, P. Sharma, R. Kumar, G. Verma and A. Saini, *Sci. Rep.*, 2020, **10**, 9441.
104 W. Zhang, H. Xu, F. Xie, X. Ma, B. Niu, M. Chen, H. Zhang, Y. Zhang and D. Long, *Nat. Commun.*, 2022, **13**, 471.
105 P. Salarizadeh, M. B. Askari and A. Di Bartolomeo, *ACS Appl. Nano Mater.*, 2022, **5**, 3361–3373.
106 Y. Meng, Y. Liu, J. He, X. Sun, A. Palmieri, Y. Gu, X. Zheng, Y. Dang, X. Huang, W. Mustain and S. L. Suib, *ACS Appl. Energy Mater.*, 2021, **4**, 5424–5433.
107 P. H. Wadekar, A. Ghosh, R. V. Khose, D. A. Pethsangave, S. Mitra and S. Some, *Electrochim. Acta*, 2020, **344**, 136147.
108 M. Lee and S. M. Paek, *Nanomaterials*, 2022, **12**, 1507.
109 R. Shu, Y. Wu, J. Zhang, Z. Wan and X. Li, *Composites, Part B*, 2020, **193**, 108027.
110 S. Y. Toh, K. S. Loh, S. K. Kamarudin and W. R. W. Daud, *Chem. Eng. J.*, 2014, **251**, 422–434.
111 E. T. Mombeshora and V. O. Nyamori, *J. Mater. Sci.: Mater. Electron.*, 2017, **28**, 18715–18734.
112 J. Regis, S. Vargas, A. Irigoyen, E. Bramasco-Rivera, J. L. Bañuelos, L. C. Delfin, A. Renteria, U. Martinez, T. Rockward and Y. Lin, *Int. J. Smart Nano Mater.*, 2021, **12**, 20–35.
113 A. K. Vivekanandan, V. Subash, S. M. Chen and S. H. Chen, *Ultrason. Sonochem.*, 2020, **68**, 105176.
114 E. F. Aboelfetoh, A. H. Gemeay and R. G. El-Sharkawy, *Environ. Monit. Assess.*, 2020, **192**, 355.
115 B. Sharma, S. Thakur, D. Trache, H. Yazdani Nezhad and V. K. Thakur, *Nanomaterials*, 2020, **10**, 1616.
116 K. Bansal, J. Singh and A. S. Dhaliwal, *Fullerenes, Nanotubes Carbon Nanostruct.*, 2022, **31**, 277–287.
117 A. M. Abdelfatah, N. El-Maghrabi, A. E. D. Mahmoud and M. Fawzy, *Sci. Rep.*, 2022, **12**, 19372.
118 D. Perumal, E. L. Albert, N. Saad, T. Y. Y. Hin, R. M. Zawawi, H. F. Teh and C. A. Che Abdullah, *Crystals*, 2022, **12**, 1539.
119 H. C. Manjunatha, Y. S. Vidya, K. N. Sridhar, L. Seenappa, B. C. Reddy, S. Manjunatha, A. N. Santhosh, N. Dhananjaya, V. Thirunavukkarasu, B. Pavithra and P. S. D. Gupta, *J. Sci.: Adv. Mater. Devices*, 2022, **7**, 100442.
120 M. F. Umar, F. Ahmad, H. Saeed, S. A. Usmani, M. Owais and M. Rafatullah, *Nanomaterials*, 2020, **10**, 1096.
121 W. Sun, Y. Hong, T. Li, H. Chu, J. Liu, L. Feng and M. Baghayeri, *Chemosphere*, 2023, **310**, 136759.
122 P. Parthipan, M. A. Al-Dosary, A. A. Al-Ghamdi and A. Subramania, *J. King Saud Univ., Sci.*, 2021, **33**, 101438.
123 P. A. Hoskeri, H. B. Muralidhara, C. R. Manjunatha, M. S. Raghu, *et al.*, *J. Electroanal. Chem.*, 2020, **858**, 113830.
124 J. Wu, Z. Lin, X. Weng, G. Owens and Z. Chen, *Chemosphere*, 2020, **246**, 125700.

125 E. Vatandost, A. Ghorbani-HasanSaraei, F. Chekin, S. Naghizadeh Raeisi and S. A. Shahidi, *Food Chem.: X*, 2020, **6**, 100085.
126 M. Buldu-Akturk, M. Toufani, A. Tufani and E. Erdem, *Nanoscale*, 2022, **14**, 3269–3278.
127 S. R. Joshi, A. Sharma, G. H. Kim and J. Jang, *Mater. Sci. Eng., C*, 2020, **108**, 110465.
128 A. Ganiyat Olatoye, J. Zhang, Q. Wang, E. Cao, W. Li, E. Oluwaseyi Fagbohun and Y. Cui, *Carbon Resour. Convers.*, 2022, **5**, 222–230.
129 G. S. Lekshmi, R. Tamilselvi, R. Geethalakshmi, S. D. Kirupha, O. Bazaka, I. Levchenko, K. Bazaka and M. Mandhakini, *J. Colloid Interface Sci.*, 2022, **608**, 294–305.
130 A. Marinoiu, M. Andrulevicius, A. Tamuleviciene, T. Tamulevicius, M. Raceanu and M. Varlam, *Appl. Surf. Sci.*, 2020, **504**, 144511.
131 E. T. Mombeshora, P. G. Ndungu, A. L. L. Jarvis and V. O. Nyamori, *Mater. Chem. Phys.*, 2018, **213**, 102–112.
132 K. O. Sodeinde, S. O. Olusanya, O. S. Lawal, M. Sriariyanun and A. A. Adediran, *Sci. Rep.*, 2022, **12**, 17054.
133 Y. M. Y. Albarqouni, S. P. Lee, G. A. M. Ali, A. S. Ethiraj, H. Algarni and K. F. Chong, *J. Nanostruct. Chem.*, 2021, **12**, 417–427.
134 A. E. D. Mahmoud, M. Hosny, N. El-Maghrabi and M. Fawzy, *Sustainable Environ. Res.*, 2022, **32**, 22.
135 M. Handayani, B. I. Suwaji, G. Ihsantia Ning Asih, T. Kusumaningsih, Y. Kusumastuti, Rochmadi and I. Anshori, *Nanocomposites*, 2022, **8**, 74–80.
136 T. Naseem, A. Zain ul, M. Waseem, M. Hafeez, S. U. Din, S. Haq and R. Mahfoz ur, *J. Inorg. Organomet. Polym. Mater.*, 2020, **30**, 3907–3919.
137 L. Lu, W. Guo, C. Chen, Q. Zhu, J. Ma, H. Wu, D. Yang, G. Yang, X. Sun and B. Han, *Green Chem.*, 2020, **22**, 6804–6808.
138 A. Mehdinia, S. Heydari and A. Jabbari, *Mater. Chem. Phys.*, 2020, **239**, 121964.
139 J. Jagiello, A. Chlanda, M. Baran, M. Gwiazda and L. Lipinska, *Nanomaterials*, 2020, **10**, 1846.
140 J. Cifuentes, C. Munoz-Camargo and J. C. Cruz, *Nanomaterials*, 2022, **12**, 2857.
141 B. Avar and M. Panigrahi, *Phys. Chem. Solid State*, 2022, **23**, 101–112.
142 B. Bashir, M. U. Khalid, M. Aadil, S. Zulfiqar, M. F. Warsi, P. O. Agboola and I. Shakir, *Ceram. Int.*, 2021, **47**, 3603–3613.
143 M. Algethami, *Mater. Res. Express*, 2022, **9**, 025001.
144 P. Das, A. B. Deoghare and S. R. Maity, *Arabian J. Sci. Eng.*, 2020, **46**, 5467–5475.
145 R. K. Singh, R. Kumar and D. P. Singh, *RSC Adv.*, 2016, **6**, 64993–65011.
146 M. Huang, Y. Wang, S. Ying, Z. Wu, W. Liu, D. Chen and C. Peng, *Sensors*, 2021, **21**, 1958.
147 J. R. do Nascimento, M. R. D'Oliveira, A. G. Veiga, C. A. Chagas and M. Schmal, *ACS Omega*, 2020, **5**, 25568–25581.
148 Z. Wu, F. Li, X. Li, Y. Yang, X. Huang and H. Li, *Nanomaterials*, 2022, **12**, 1581.
149 N. Belachew, M. H. Kahsay, A. Tadesse and K. Basavaiah, *J. Environ. Chem. Eng.*, 2020, **8**, 104106.
150 P. García Lebière, A. Pérez del Pino, C. Logofatu and E. György, *Appl. Surf. Sci.*, 2021, **563**, 150234.
151 D. d. L. Alves, A. O. da Silva, S. N. Monteiro, R. P. Weber, F. J. H. T. V. Ramos and L. R. Menezes, *J. Mater. Res. Technol.*, 2022, **20**, 4241–4255.
152 Y. Wang, G. Hu, Y. Cao, Z. Peng and K. Du, *Mater. Chem. Phys.*, 2021, **265**, 124523.
153 M. Pinzón, O. Avilés-García, A. R. de la Osa, A. de Lucas-Consuegra, P. Sánchez and A. Romero, *Sustainable Chem. Pharm.*, 2022, **25**, 100615.
154 S. Roy Chowdhury and T. Maiyalagan, *ACS Omega*, 2022, **7**, 19183–19192.
155 S. S. Naik, S. J. Lee, T. Begildayeva, Y. Yu, H. Lee and M. Y. Choi, *Environ. Pollut.*, 2020, **266**, 115247.
156 Z. Huo, H. Wu, Q. Song, Z. Zhou, T. Wang, J. Xie and H. Qu, *Carbohydr. Polym.*, 2021, **256**, 117575.
157 P. Karthikeyan, S. S. D. Elanchezhiyan, H. A. T. Banu, M. Hasmath Farzana and C. M. Park, *Chemosphere*, 2021, **276**, 130200.
158 W. Peng, H. Chen, W. Wang, Y. Huang and G. Han, *Curr. Appl. Phys.*, 2020, **20**, 304–309.
159 A. Lim Teik Zheng, T. Phromsatit, S. Boonyuen and Y. Andou, *FlatChem*, 2020, **23**, 100174.
160 G. Bharath, N. Arora, A. Hai, F. Banat, D. Savariraj, H. Taher and R. V. Mangalaraja, *Electrochim. Acta*, 2020, **337**, 135668.
161 Z. Said, M. A. Abdelkareem, H. Rezk, A. M. Nassef and H. Z. Atwany, *Powder Technol.*, 2020, **364**, 795–809.
162 H. Qian, J. Wang and L. Yan, *J. Bioresour. Bioprod.*, 2020, **5**, 204–210.
163 R. Shu, J. Zhang, C. Guo, Y. Wu, Z. Wan, J. Shi, Y. Liu and M. Zheng, *Chem. Eng. J.*, 2020, **384**, 123266.
164 Y. Wu, W. Zhao, Y. Qiang, Z. Chen, L. Wang, X. Gao and Z. Fang, *Carbon*, 2020, **159**, 292–302.
165 Y. Xie, *Fullerenes, Nanotubes Carbon Nanostruct.*, 2021, **30**, 619–625.
166 H. Nosrati, R. Sarraf-Mamoory, D. Q. S. Le, R. Zolfaghari Emameh, M. Canillas Perez and C. E. Bunger, *Sci. Rep.*, 2020, **10**, 8552.
167 N. Li, R. Shu, J. Zhang and Y. Wu, *J. Colloid Interface Sci.*, 2021, **596**, 364–375.
168 A. G. Ramu, A. Umar, A. A. Ibrahim, H. Algadi, Y. S. A. Ibrahim, Y. Wang, M. M. Hanafiah, P. Shanmugam and D. Choi, *Environ. Res.*, 2021, **200**, 111366.
169 P. K. Kahriz, H. Mahdavi, A. Ehsani, A. A. Heidari and M. Bigdeloo, *Electrochim. Acta*, 2020, **354**, 136736.
170 R. Shu, C. Zhao, J. Zhang, W. Liu, X. Cao, Y. Li and S. Liu, *J. Colloid Interface Sci.*, 2021, **585**, 538–548.
171 J. Ma, Y. Yamamoto, C. Su, S. Badhulika, C. Fukuhara and C. Y. Kong, *Electrochim. Acta*, 2021, **386**, 138439.
172 W. Geng, W. Li, L. Liu, J. Liu, L. Liu and X. Kong, *Fuel*, 2020, **259**, 116267.
173 M. Shahid, T. R. Katugampalage, M. Khalid, W. Ahmed, C. Kaewsaneha, P. Sreearunothai and P. Opaprakasit, *Sci. Rep.*, 2022, **12**, 19043.

174 S. Kashyap, V. Kumar, S. Abraham, S. Umrao, S. Singh, A. Kamath, R. Ms, A. Srivastava and P. S. Saxena, *Austin J. Biosens. Bioelectron.*, 2017, **3**, 1026.
175 P. S. Selvamani, J. J. Vijaya, L. J. Kennedy, B. Saravanakumar, N. C. S. Selvam and P. J. Sophia, *J. Electroanal. Chem.*, 2021, **895**, 115401.
176 J. Zhao, J. Zhang, H. Yin, Y. Zhao, G. Xu, J. Yuan, X. Mo, J. Tang and F. Wang, *Nanomaterials*, 2022, **12**, 1210.
177 M. M. Atta, M. I. A. Abdel Maksoud, O. I. Sallam and A. S. Awed, *J. Mater. Sci.: Mater. Electron.*, 2021, **32**, 3688–3698.
178 S. Kianfar, A. N. Golikand and B. ZareNezhad, *J. Nanostruct. Chem.*, 2020, **11**, 287–299.
179 R. Jakhar, J. E. Yap and R. Joshi, *Carbon*, 2020, **170**, 277–293.
180 E. Murray, S. Sayyar, B. C. Thompson, R. Gorkin III, D. L. Officer and G. G. Wallace, *RSC Adv.*, 2015, **5**, 45284–45290.
181 J. Kang, Y. Ko, J. P. Kim, J. Y. Kim, J. Kim, O. Kwon, K. C. Kim and D. W. Kim, *Nat. Commun.*, 2023, **14**, 901.
182 V. V. Chaban and O. V. Prezhdo, *Nanoscale*, 2017, **9**, 4024–4033.
183 B. B. Palei, T. Dash and S. K. Biswal, *IOP Conf. Ser.: Mater. Sci. Eng.*, 2020, **872**, 012158.
184 K. Kakaei and M. Rahnavardi, *Renewable Energy*, 2021, **163**, 1277–1286.
185 S. D. Bukkitgar, N. P. Shetti, K. R. Reddy, T. A. Saleh and T. M. Aminabhavi, *FlatChem*, 2020, **23**, 100183.